Cell

Resource

Whole-body molecular and cellular mapping of the laboratory mouse

Graphical abstract

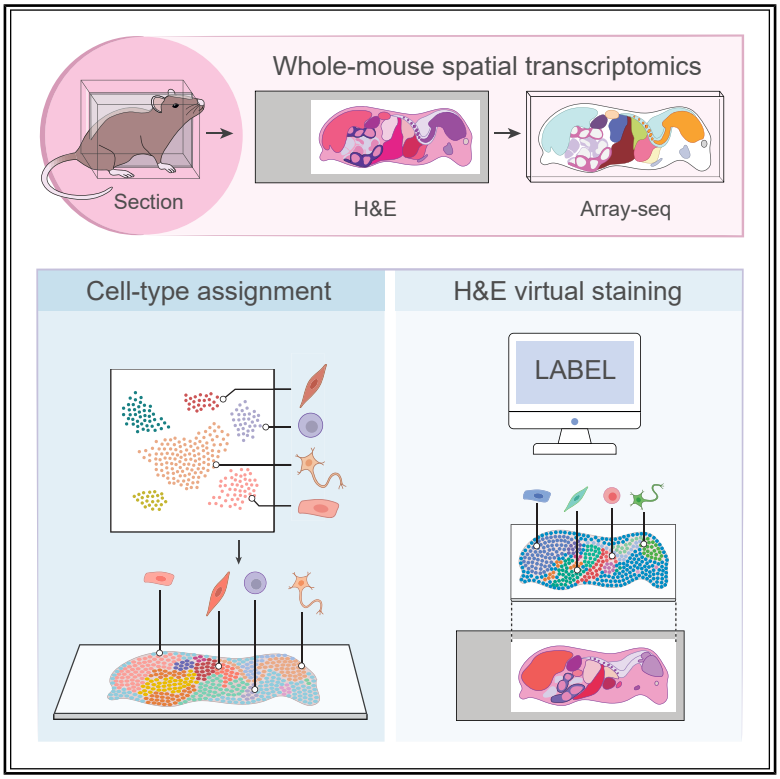

Authors

Margarette H. Clevenger, Denis Cipurko, Ashwini Patil, ..., Tadafumi Kawamoto, Feng Bao, Nicolas Chevrier

Correspondence

fbao@fudan.edu.cn (F.B.), nchevrier@uchicago.edu (N.C.)

In brief

A scalable experimental and computational platform for mapping all organs and cell types in the mouse body, enabling comprehensive analysis of tissue organization and disease responses.

Highlights

- Spatial transcriptomics profiles of whole-body sections from 6-week-old mice
- LABEL algorithm annotates organs, tissues, and cell types on H&E images
- Whole-body mapping reveals systemic inflammation properties in mouse endotoxemia
- Unified framework enabling body-wide spatiomolecular studies in the laboratory mouse

Clevenger et al., 2026, Cell *189*, 1–18
May 28, 2026
https://doi.org/10.1016/j.cell.2026.03.006

CellPress

Please cite this article in press as: Clevenger et al., Whole-body molecular and cellular mapping of the laboratory mouse, Cell (2026), https://doi.org/10.1016/j.cell.2026.03.006

Cell

CellPress

Resource

Whole-body molecular and cellular mapping of the laboratory mouse

Margarette H. Clevenger,[1,7] Denis Cipurko,[1,7] Ashwini Patil,[2,7] Bohan Li,[3,7] Michihiro Takahama,[1,6,7] Linghan Mei,[1] Madison Plaster,[1] Gabriella Richey,[1] Tadafumi Kawamoto,[4] Feng Bao,[5,*] and Nicolas Chevrier[1,8,*]

[1]Pritzker School of Molecular Engineering, the University of Chicago, Chicago, IL 60637, USA
[2]Combinatics Inc., Chiba 272-0824, Japan
[3]School of Artificial Intelligence, Beihang University, Beijing 102206, China
[4]School of Dental Medicine, Tsurumi University, Yokohama 230-8501, Japan
[5]College of Future Information Technology, Fudan University, Shanghai 200433, China
[6]Present address: Laboratory of Bioresponse Regulation, Graduate School of Pharmaceutical Sciences, University of Osaka, Osaka 565-0871, Japan
[7]These authors contributed equally
[8]Lead contact
*Correspondence: fbao@fudan.edu.cn (F.B.), nchevrier@uchicago.edu (N.C.)
https://doi.org/10.1016/j.cell.2026.03.006

SUMMARY

The laboratory mouse is a key model system for biomedical research, yet body-wide measurement tools are lacking. Here, we generate spatiotranscriptomics profiles of whole-mouse sections that accurately capture histological regions. We spatially assign 379 cell types across whole-mouse section profiles by building a reference dataset of 59M single cells coupled with a scalable computational method for cell-type assignment. Moreover, we exploit these whole-mouse profiles to create a machine learning pipeline, LABEL, which enables pan-body annotation of tissues and cell types on histology images from H&E-stained sections. Lastly, we apply whole-mouse spatial profiling to map systemic inflammation in endotoxemia, which delineates organism-wide changes in gene expression programs across tissues and cell types. Together, our work paves the way for body-wide studies of the molecular and cellular processes that govern the organismal biology of the laboratory mouse across space, time, and conditions.

INTRODUCTION

The laboratory mouse has been a pillar model system in biomedical research for over a century, leading to countless groundbreaking discoveries across all fields of basic and clinical sciences. The ease of using mice as a mammalian model system, the close resemblance between the genes, anatomy, and physiology of mice and humans, and the ever-expanding toolkit for mouse genetic engineering have converged to propel the generation of mouse models of human diseases affecting virtually all organ systems. Yet, our knowledge of the mechanisms underlying healthy and disease processes across all cell types and organ systems of the mouse body remains incomplete. This fundamental gap in knowledge is partly due to a lack of measurement tools that can capture detailed spatiomolecular views of all tissues and cell types of the mouse body at once. Tackling this challenge will help write the next chapter of the mouse model by defining its systems biology across scales spanning molecules, cells, tissues, organs, and the whole organism.

To fulfill this vision, there is a critical need to develop tools that can measure genome-wide changes in the body-wide spatiomolecular makeup of adult mice across changing homeostatic, disease, therapy, or genetic conditions. Pioneering studies used whole-mouse sections to track the body-wide spatial distribution of viral transcripts using *in situ* hybridization or memory lymphocytes using immunohistology.[1,2] In addition, recent efforts led to methods for the optical clearing of the whole mouse body followed by imaging, enabling the body-wide visualization of fluorescent reporter or immunostaining signals for specific cell types or proteins.[3–7] However, these body-wide approaches are not compatible with genome-wide measurements in gene expression regulation. Conversely, recent advances in genome-wide measurements of spatial gene expression across tissue sections are not compatible with body-wide sections from adult mice because (1) surface areas for spatial profiling are too small, (2) tools for the histological sectioning of whole, adult mice that preserve tissue and RNA integrity are lacking,[8,9] and (3) computational methods for the pan-body analysis of mouse organs and cell types need to be developed.

Here, we developed histological and computational methods for the spatiotranscriptomic profiling of whole-mouse sections using Array-seq, a spatial transcriptomics platform that we recently reported.[10] We obtained histology and spatiotranscriptomics maps of whole-mouse sections, which accurately

Please cite this article in press as: Clevenger et al., Whole-body molecular and cellular mapping of the laboratory mouse, Cell (2026), https://doi.org/10.1016/j.cell.2026.03.006

captured the molecular and tissue architectures of 16 key murine organ systems and additional small tissue structures within their native anatomical contexts. To spatially assign cell types onto whole-mouse profiles, we built a scalable computational framework using a curated reference dataset of 59M cells from 466 single-cell RNA sequencing studies, mapping 379 cell types across the ~5M nuclei of our whole-mouse sections. Next, we developed LABEL, a whole-mouse annotation model that combines a pre-trained pathology foundation model, UNI,[11] with a spatially aware K-nearest neighbors (KNNs) classifier, enabling automated annotation of organs, tissues, and cell types on images from H&E-stained whole-mouse sections. Last, to illustrate the power of whole-mouse spatial profiling to study disease, we focused on systemic inflammation in a mouse model of endotoxemia. We uncovered body-wide changes in cell states and compositions in response to inflammation, including gene programs controlled by STAT1 and IRF1 across hematopoietic and non-hematopoietic cells.

Taken together, our work established experimental and computational tools and resources for the body-wide, genome-wide spatiomolecular profiling of laboratory mice, which are broadly applicable to all fields of basic and pre-clinical research using mouse models.

RESULTS

Spatial transcriptomes of whole-mouse sections accurately capture tissue subregions

We developed a method for the body-wide sectioning of mice that is compatible with both the size of ~6-week-old, C57BL/6J mice, the most commonly used laboratory mouse strain and age,[12] and downstream spatial transcriptomics profiling using Array-seq (Figure 1A).[10] Resulting whole-mouse sections maintained histological structures with little to no damage across tissues, including the eye, intestinal mucosa, spleen, and bone marrow (Figures S1A–1E), and RNA integrity after section transfer onto glass (Figure S1F) (STAR Methods).[13–15] We generated whole-body sections from two independent mice, which were stained with hematoxylin and eosin (H&E) and imaged prior to Array-seq profiling (Figures 1B and 1C; Figures S1G–S1L). The two whole-mouse sections covered 588,299 (replicate 1) and 610,689 (replicate 2) spots per Array-seq slide, respectively. We detected 662.3 genes ±2.9 SD and 1,241.4 unique molecular identifiers (UMIs) ± 19.2 SD per spot on average across both replicates and all tissues present in the sections. Spatial patterns of expression intensity, measured by total UMIs, total transcripts, and ribosomal protein or mitochondrial genes per spot, reflected expected variations across organs for these RNA species (Figure 1C; Figures S1G and S1I–S1L). For example, UMIs per spot were highest in liver tissue, whereas bone marrow and skin were lowest (Figures S1G and S1I), and mitochondrial RNA content was highest in metabolically active heart and fat tissues (Figures S1G and S1K).

Next, we found that spatiotranscriptomic clusters correctly identified the main organ types of the body (Figure S1L), as confirmed by the expression of known organ-specific marker genes (Figures S1M and S1N). Organ-specific spatial profiles correlated significantly between our two whole-mouse sections (Pearson's coefficient 0.968 ± 0.0129 SD for n = 16 tissues) and with bulk RNA-seq from matching tissues (Pearson's coefficient 0.790 ± 0.0405 SD for n = 12 tissues) (Figures S1O and S1P). Moreover, clusters accurately recapitulated the histological features and tissue subregions detectable by H&E staining across all 16 major organ types tested (Figure 1D; Figure S2A), as corroborated by the spatial expression of marker genes across subregions (Figure S2B). For example, our data on the brain correctly identified the caudoputamen, cerebral cortex, fiber tracts, and ventricles (Figure S2C), and cerebellar layers, as shown by the expression of *Mobp*, *Pcp2*, and *Nrep* in the fiber tracts, granular layer, and molecular layer, respectively (Figure 1E).[16] Our data on the stomach identified the foveolar epithelium and the parietal cell and chief cell-rich regions of stomach gastric glands responsible for hydrochloric acid and pepsinogen secretion correctly, respectively (Figure S2D).[17] In the small intestine, tissue layers were correctly delineated by our data as demonstrated by the spatial distribution of marker genes such as *Defa30* for muscularis mucosa and *Oat* and *Krt20* for proximal and distal enterocytes, respectively (Figure 1F). In the liver, the expression of *Sds*, *Cyp2a5*, and *Glul* mirrored the transition from periportal to pericentral hepatocytes in liver lobules (Figure 1G).[18]

Thus, by combining whole-mouse sectioning with Array-seq, we generated spatiotranscriptomic maps of whole-mouse sections that accurately captured the histological subregions of all the major organs tested.

Spatial mapping of cell types across whole-mouse sections

To systematically identify the spatial assignment of cell types across whole-mouse sections, we developed a computational method to infer the cell-type composition of each Array-seq spot under tissue (Figure 2A; STAR Methods). We used the CellKb database to assemble a curated reference dataset of ~59M single cells from 466 single-cell gene expression studies spanning all the major 16 organ systems in our sections (Tables S1A and S1B).[19] Using this reference single-cell dataset, we defined gene sets specific to 495 granular cell types encompassing these 16 organ types. In addition, we classified these 495 granular cell types into 79 broad and 30 core cell types to facilitate downstream analyses and visualizations (Table S1C). We detected 67.3% (333/495) and 69.1% (342/495) of our reference granular cell types across the 16 main organ systems of our two whole-mouse spatial profiles (1,195,065 spots in total), which we displayed by focusing on the top 48 broad cell types by proportion (Figure 2B; Figures S3A–S3C; Tables S1D and S1E).

We found that these broad cell-type assignments were consistent with the expression patterns of marker genes for these cell types (Figure S3D). Skeletal muscle cells were the most represented, covering 44.18% (259,641/587,691) and 32.57% (197,802/607,374) of all spots in replicates 1 and 2, respectively, as expected based on the H&E stains of the whole-body sections (Figures 1B and 2B; Figures S3A and S3B). After muscle cells, hepatocytes, and gut epithelial cells (specialized epithelial cells) were detected in 8.8% and 7.8% of all spots in replicates 1 and 2, respectively (Figure 2B; Figures S3A and S3B). Cell types with

Please cite this article in press as: Clevenger et al., Whole-body molecular and cellular mapping of the laboratory mouse, Cell (2026), https://doi.org/10.1016/j.cell.2026.03.006

CellPress

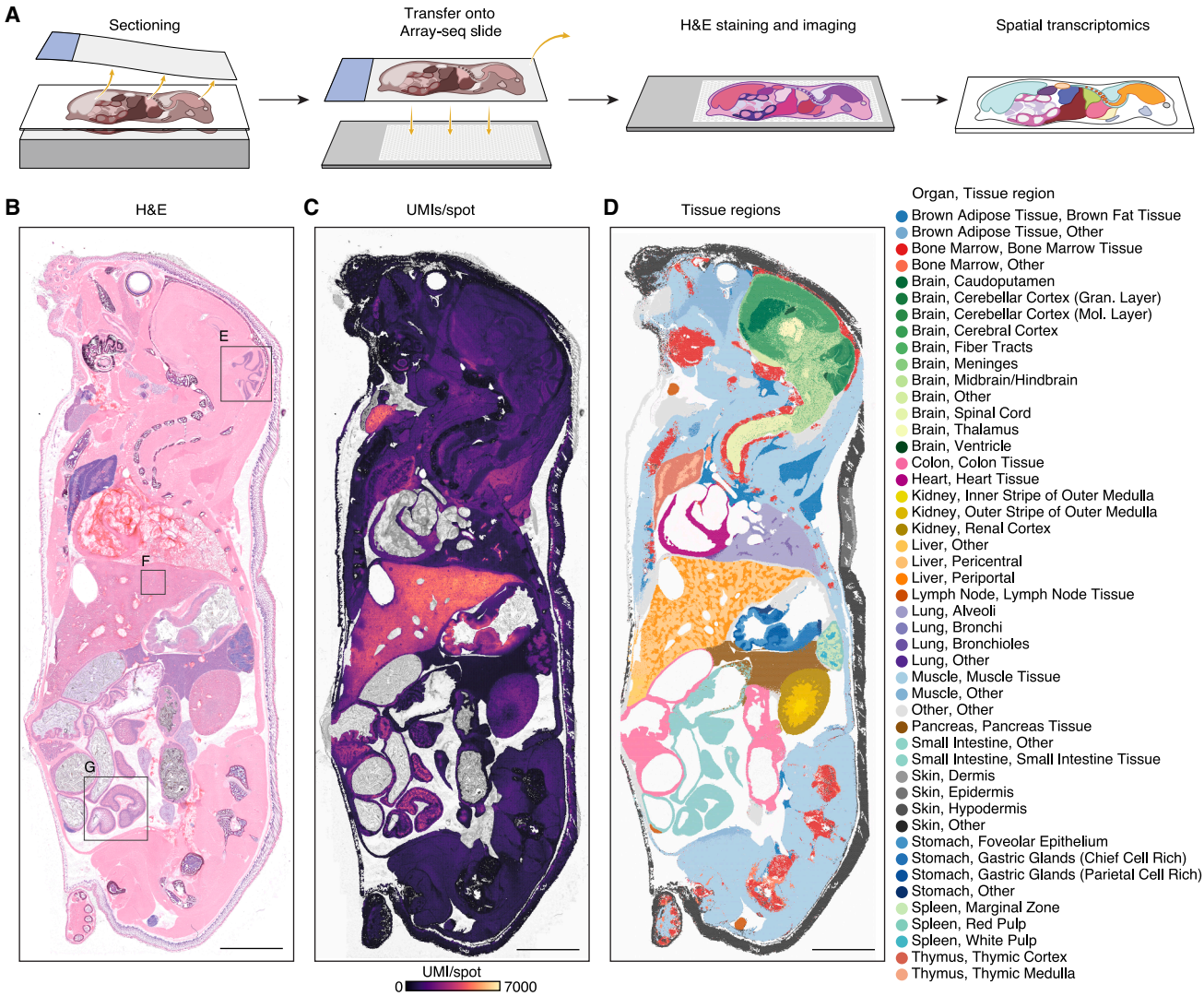

Figure 1. Spatial transcriptomics of whole-mouse sections using Array-seq

(A) Schematic overview of the experimental workflow.

(B–D) Whole-mouse section H&E image (B) overlaid with unique molecular identifier (UMI) counts per spot (C) or unsupervised clusters annotated with indicated organs and tissue regions (D).

(E–G) Magnified images of the insets in (B) from brain (E), small intestine (F), and liver (G) tissues showing H&E images (left) and scaled $\log_{10}$ expression of indicated marker genes (right).

Scale bars: 5 mm (B–D); 500 μm (E–G).

Gran, granular; Mol, molecular; ML, molecular layer; FT, fiber tracts; GL, granular layer; DE, distal epithelium; PE, proximal epithelium; MM, muscularis mucosae; PV, periportal vein; CV, central vein.

See also Figures S1 and S2.

Please cite this article in press as: Clevenger et al., Whole-body molecular and cellular mapping of the laboratory mouse, Cell (2026), https://doi.org/10.1016/j.cell.2026.03.006

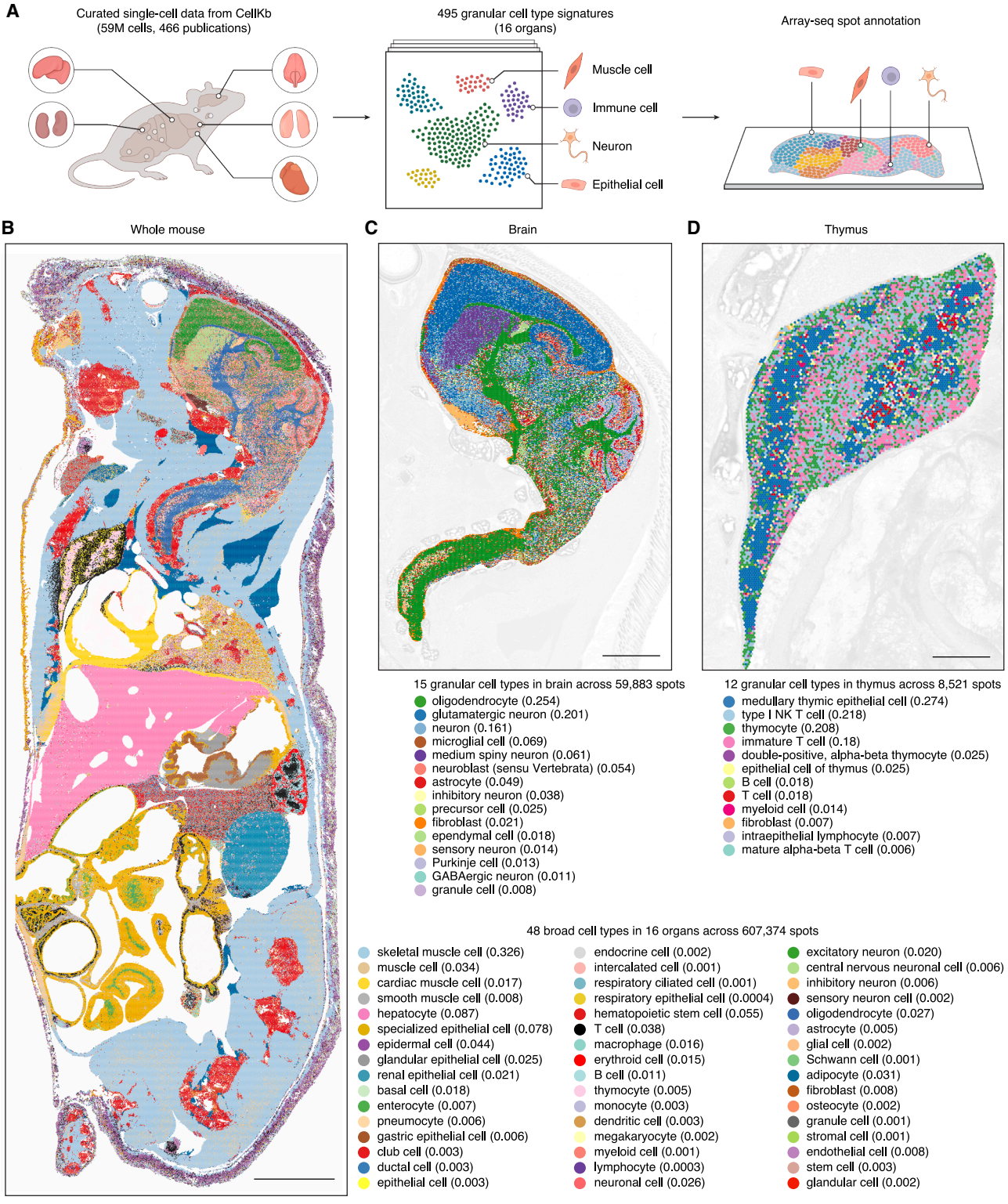

(legend on next page)

Please cite this article in press as: Clevenger et al., Whole-body molecular and cellular mapping of the laboratory mouse, Cell (2026), https://doi.org/10.1016/j.cell.2026.03.006

lower abundance were also detected accurately, including osteocytes (0.2%) in bone such as the skull, spine, and hip bones, or endothelial cells (0.7%) in brain, brown fat, colon, heart, kidney, liver, lung, muscle, pancreas, skin, and thymus (Figure 2B; Figures S3A and S3B). All hematopoietic cell types combined represented ~12.27% of all spots (146,646/1,195,065 for two sections), including 6.12% in lymphoid organs (thymus, spleen, and bone marrow) and 6.15% in non-lymphoid tissues at steady state (Figure 2B; Figures S3A and S3B). Furthermore, our cell-type analysis recapitulated the expected cell-type composition of each organ. For example, the most abundant broad cell types in brown fat, heart, and kidney were, respectively, adipocytes (98.41%, 30,948/31,449 of organ-specific spots), cardiac muscle cells (94.69%, 18,840/19,897), and renal epithelial cells (86.52%, 27,455/31,733) (Figure S3B). Collectively, T cell subsets in our reference annotation data (48/495 total cell types) were abundant in lymph node (29.13%, 998/3,426 of organ-specific spots), spleen (37.42%, 3,678/9,828), and thymus (64.82%, 6,663/10,280), as well as in non-lymphoid tissues such as colon (17.15%, 6,661/38,844) and skin (12.51%, 15,104/120,754), and encompassed a total of 27 T cell subsets out of the 48 present in our reference (Figure S3B).

To assess the robustness of our computational approach for spot-level cell-type inference, we benchmarked our method against existing tools for cell-type assignment in spatial transcriptomics datasets, including robust cell type decomposition (RCTD),[20] cell2location,[21] and conditional autoregressive-based deconvolution (CARD).[22] All three methods yielded concordant spot-level annotations with our curated reference-derived annotations across spleen, lung, liver, and kidney (Figure S3E and S3F). RCTD and CARD results were closest to our method overall (mean concordance = 93.7% and 91.4%, respectively), followed by cell2location (87.8%), and concordance was highest in spleen (RCTD: 97.8%; CARD: 97.3%) and liver (RCTD: 96.3%; CARD: 94.9%) (Figure S3F).

The spatial distribution of cell types annotated across Array-seq spots under whole-mouse sections was correctly assigned to histological subregions. For example, in the cerebellar cortex of the brain, the Purkinje cell layer, which is 20–25 μm thick[23] or 1 Purkinje soma in width,[24] was accurately detected in our spatial data between the granular and molecular layers of the cerebellar cortex, as corroborated by the spatial expression pattern of the Purkinje cell marker gene *Calb1* (Figure 2C; Figure S3G). In the thymus, immature, double-positive (DP) thymocytes expressing *Rag1* were found in the thymic cortex, in which high levels of *Ccr9* and its ligand *Ccl25* were also detected, as expected (Figure 2D; Figures S3H and S3I).[25] Moreover, positively selected thymocytes with high *Ccr7* expression and *Ccl21a*-expressing, medullary thymic epithelial cells were correctly assigned to the thymic medulla (Figures S3H and S3I).[26]

Next, we asked whether our data could resolve finer tissue structures by clustering spots under tissue for the 16 major organs and the unannotated tissues identified as "other" in our initial analyses (Figure 1D; Figures S1L, S4A, and S4B; STAR Methods). We identified distinct clusters corresponding to the major and minor salivary glands, reflecting transcriptional differences between gland types rather than serous versus mucous composition (Figures S4A–S4C). Major glands expressed *Klk1* and *Muc19*, marking serous and mixed acinar populations, whereas minor glands uniquely expressed *Muc5b*, a mucin characteristic of the secretory epithelium (Figure S4D). The eye and its associated Harderian gland formed discrete clusters and expressed known cell-type marker genes, including *Rho* in photoreceptor outer segments, *Snap25* in retinal neuronal layers, and *Urod* in Harderian acinar epithelium associated with the gland's role in porphyrin synthesis (Figure S4E).[27] In the pancreas, we detected pancreatic islets expressing *Ins2*, *Sst*, and *Gcg* genes in β, δ, and α cells, respectively (Figure S4F).

Taken together, our analyses yielded a body-wide map of the composition and localization of mouse cell types across histological regions, including fine tissue layers.

LABEL, a model for the virtual staining of H&E images

We asked whether our whole-mouse histology images, annotated with organ, tissue, and cell-type information derived from spatiomolecular data, could train a predictive model for automated labeling of histology images without the need for sequencing. To do so, we developed LABEL, a hybrid model, by (1) using a pre-trained foundation model of pathology images, UNI,[11] for unsupervised feature extraction from whole-mouse H&E image patches, and (2) creating a spatially aware KNNs classifier (Figure 3A; STAR Methods). We trained and evaluated the performance of LABEL using (1) an "in-distribution" approach using 3% of all H&E image patches matching whole-mouse spatial profiles for training and an independent 20% for testing; and (2) a "leave-one-out" strategy excluding one whole-mouse section at a time from training, which was then used for testing (STAR Methods).

At the organ level, our model yielded a mean accuracy score of 0.91 across the 16 organ systems tested using the "in-distribution" approach described above, with mean scores above 0.95 for most organs, including brain, liver, and kidney (Figure 3B; Figures S5A and S5B; Table S2A). Bone marrow and brown fat exhibited the lowest scores, 0.72 and 0.73, respectively, which could be attributed to insufficient representation of these organs in our data (Figure S5B). The more stringent "leave-one-out" approach led to a mean accuracy score of 0.71 across all tested organs, with brain, liver, small intestine, thymus, skin, and muscle above 0.80 (Figure S5C; Table S2B). For tissue subregions, we obtained a mean accuracy score of 0.73 across 33 unique

Figure 2. Spatial cell-type annotation of whole-mouse section Array-seq data

(A) Schematic overview of the computational workflow.

(B–D) Spatial annotation of cell types (colors) across all spots of the Array-seq slide under the whole-mouse section. Shown are broad cell types across 16 main organ types in a whole-mouse section (B), and granular cell types in the brain (C) and thymus (D). Each spot was assigned the cell type with the highest inferred proportion. Numbers in parentheses indicate the proportion of a cell type across all spots for the whole-mouse section (B) or indicated organs (C and D).

Scale bars: 5 mm (B); 1 mm (C and D).

See also Figures S3 and S4 and Table S1.

Please cite this article in press as: Clevenger et al., Whole-body molecular and cellular mapping of the laboratory mouse, Cell (2026), https://doi.org/10.1016/j.cell.2026.03.006

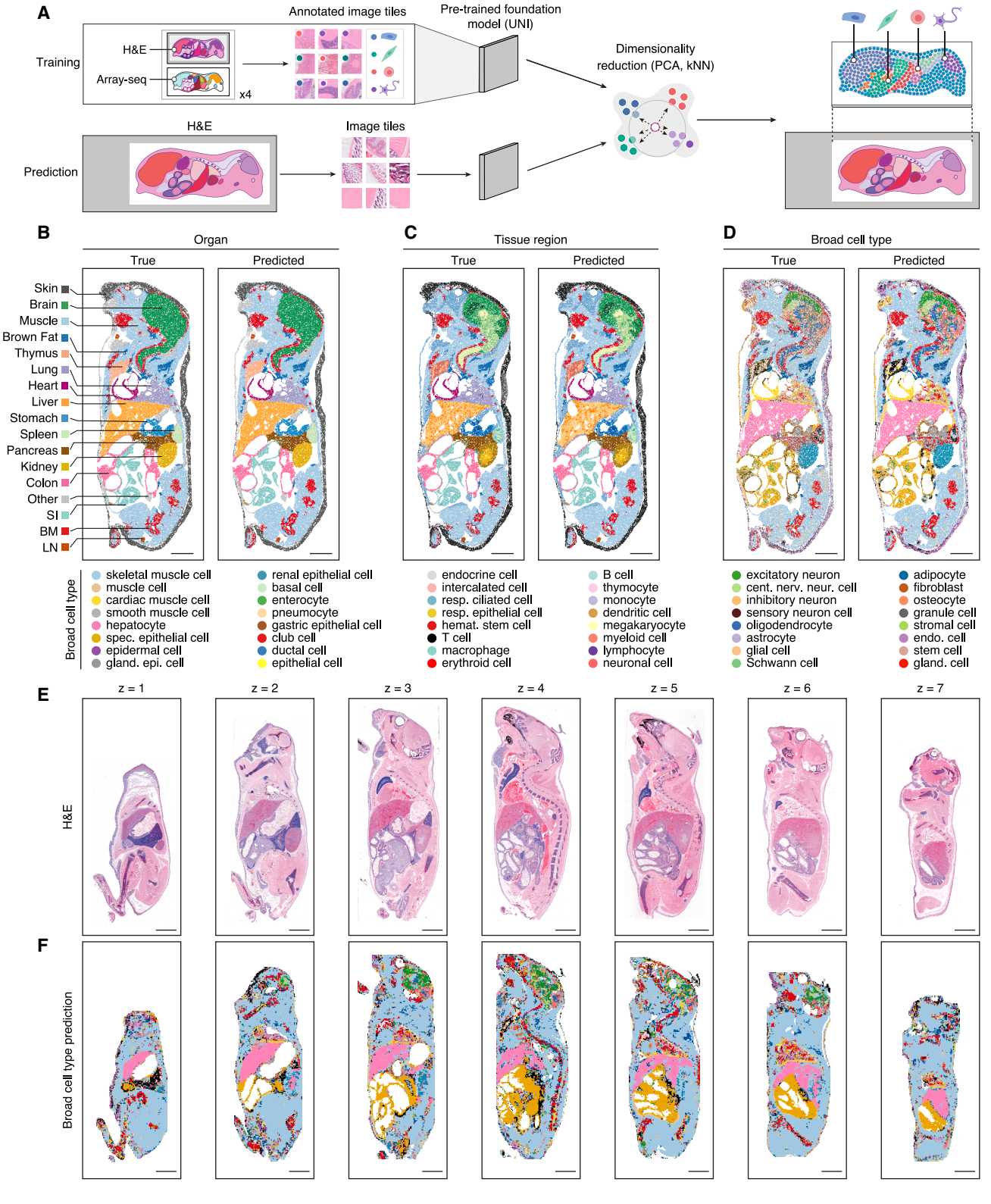

(legend on next page)

Please cite this article in press as: Clevenger et al., Whole-body molecular and cellular mapping of the laboratory mouse, Cell (2026), https://doi.org/10.1016/j.cell.2026.03.006

tissue subregions using the "in-distribution" approach, including in heart, colon, and lung which exceeded 0.93, whereas less represented subregions displayed lower accuracy scores such as lung bronchioles (0.28), splenic white pulp (0.39), and brain ventricles (0.47) (Figure 3C; Figures S5D and S5E; Table S2C). We obtained a mean accuracy score of 47.4 across these 33 tissue subregions using the "leave-one-out" approach, including 27.3% (9/33) of subregions above 0.7 (Figure S5F; Table S2D).

At the cell-type level, we focused on the 42 broad cell types from our classification with >0.1% abundance in our data (Table S2E; STAR Methods). The virtual annotation of broad cell types on H&E images using LABEL was accurate for some cell types, including hepatocytes (0.98), renal epithelial cells (0.94), or skeletal muscle cells (0.9), whereas several immune and progenitor cell types had mean accuracy scores near zero (Figure 3D; Figures S5G and S5H). Out of the 42 broad cell types tested, 38.1% (16/42) displayed accuracy scores above 0.5, including adipocytes or epithelial (hepatocytes, renal epithelium), muscle (skeletal, cardiac, smooth), and neural (neurons, glia) cell types (Figure 3D; Figures S5G and S5H). Our results with the "leave-one-out" training approach led to 14.3% (6/42) of broad cell types with accuracy scores over 0.5, with the highest scores for hepatocytes (0.85), skeletal muscle cells (0.79), and renal epithelial cells (0.68) (Figure S5I; Table S2F).

Next, we used LABEL to annotate organs, tissues, and cell types onto H&E images from whole-mouse sections. We predicted most organs, including the brain, liver, lungs, muscle, and gut, with high accuracy based on visual examination (Figures S5J and S5K). However, organ systems absent from the training data or similar in morphology were occasionally mislabeled (e.g., cardiac tissue as muscle, salivary glands as kidney) (Figures S5J and S5K). Tissue subregions were accurately annotated in many cases, including brain subregions and thymic and renal cortex and medulla (Figure S5L). Lastly, LABEL correctly annotated several broad cell types, such as skeletal muscle cells in the body wall musculature, hepatocytes in the liver, neurons in the brain, epidermal cells in the skin, and T cells and hematopoietic stem cells in the thymus and bone marrow, respectively (Figures 3E and 3F). Epithelial cell subtypes were accurately identified in many cases, including gastric epithelial cells in the stomach lining, specialized gut epithelial cells in the colon and small intestine linings, renal epithelial cells in the kidney, and club cells in the lung (Figures 3E and 3F).

Thus, LABEL enabled fine-grained annotation of multiple organs, tissues, and broad cell types on H&E images with high accuracy and without the need for sequencing.

Body-wide mapping of systemic inflammation

We mapped the spatial transcriptomes of whole-mouse sections from mice injected with a sublethal dose of lipopolysaccharide (LPS) to mimic systemic bacterial inflammation (Figure 4A).[28] We found 5,143 genes that were differentially expressed between LPS and control across 37 tissue subregions spanning 16 organ types (Figures 4B and 4C; Table S3; STAR Methods). We found a strong correlation between bulk and spatial datasets in terms of the identity of LPS-regulated genes and the magnitude of the detected changes in expression across all 13 tissues tested by bulk and spatial measurements (Figure S6A). Genes found to be differentially regulated in spatial but not in bulk and vice versa likely reflected differences between measurement tools and associated statistical methods (STAR Methods).

Next, we examined the spatial expression of genes linked to systemic inflammation, such as acute-phase proteins, chemokines, and interferon-stimulated genes (ISGs). The expression of genes encoding serum amyloid A (SAA) proteins 1, 2, and 3—common biomarkers of systemic inflammatory conditions—was all strongly upregulated in the liver, while *Saa1* was also found in the gut, *Saa2* in the kidney, and *Saa3* in virtually all tissues and cells of the body (Figure 4D). Chemokines displayed various patterns of spatial expression during endotoxemia, such as *Ccl5* and *Cxcl9* (broadly upregulated), *Ccl12* (highest in brain and thymus), and *Cxcl13* (mostly in the splenic marginal zone and the skin basal layer) (Figure 4E; Figure S6B). The ISG *Irgm1* was broadly induced upon LPS treatment in the kidney, liver, lung, or heart, which may help explain its protective effects against LPS-induced shock (Figure S6C).[29]

Lastly, we investigated how endotoxemia reshaped intercellular communications via secreted and membrane-bound factors by quantifying ligand-receptor (L-R) signaling within each major organ system in our data (STAR Methods). Several L-R signaling pathways were broadly increased across organs upon LPS injection, including vascular adhesion pathways (e.g., ICAM, PECAM1/2, VCAM, CD34, selectins), chemokine (e.g., CXCL, CCL) and cytokine (e.g., TNF, IL-1, CSF3, CSF) signaling, or matrix remodeling pathways (e.g., PLAU, MMP, ANGPT, ANGPTL, PDGF, KLK), reflecting the body-wide inflammation in endotoxemia (Figure S6D; Table S4A). We observed a concomitant increase in anti-inflammatory L-R pathways (e.g., CEACAM, CD200, IL-10, CD39, PD-L1, TGF-β, LAIR1), likely encompassing immunoregulatory programs limiting inflammation (Figure S6D; Table S4A).[30,31] LPS also triggered an epithelial/endothelial remodeling response across visceral and barrier tissues (e.g., CDH1, OCLN, CLDN, JAM, ESAM pathways) (Figure S6D; Table S4A). Moreover, the L-R pairs CXCL2-CXCR2, CXCL5-CXCR2, or CSF3-CSF3R, known regulators of neutrophil activation and migration,[32–36] were highly increased in lung, liver, brown fat, and bone marrow (Figure S6E; Table S4B). L-R pairs CCL8-CCR1, CCL8-CCR5, and CCL19-CCR7 were elevated upon LPS in lung, brown fat, and lung and liver, respectively (Figure S6E; Table S4B), pointing to

Figure 3. Virtual annotation of organs, tissues, and cell types onto whole-mouse H&E images

(A) Schematic overview of the computational workflow for our LABEL algorithm.

(B–D) Whole-mouse spatial transcriptomics data labeled with ground truth and LABEL-predicted identities per spot at the organ (B), tissue region (C), and broad cell type (D) levels.

(E and F) H&E-stained, whole-mouse sections from a single 6-week-old animal at various depths (E) annotated with broad cell types (colors) using LABEL (F). Scale bars: 5 mm (B–F).

See also Figure S5 and Table S2.

Please cite this article in press as: Clevenger et al., Whole-body molecular and cellular mapping of the laboratory mouse, Cell (2026), https://doi.org/10.1016/j.cell.2026.03.006

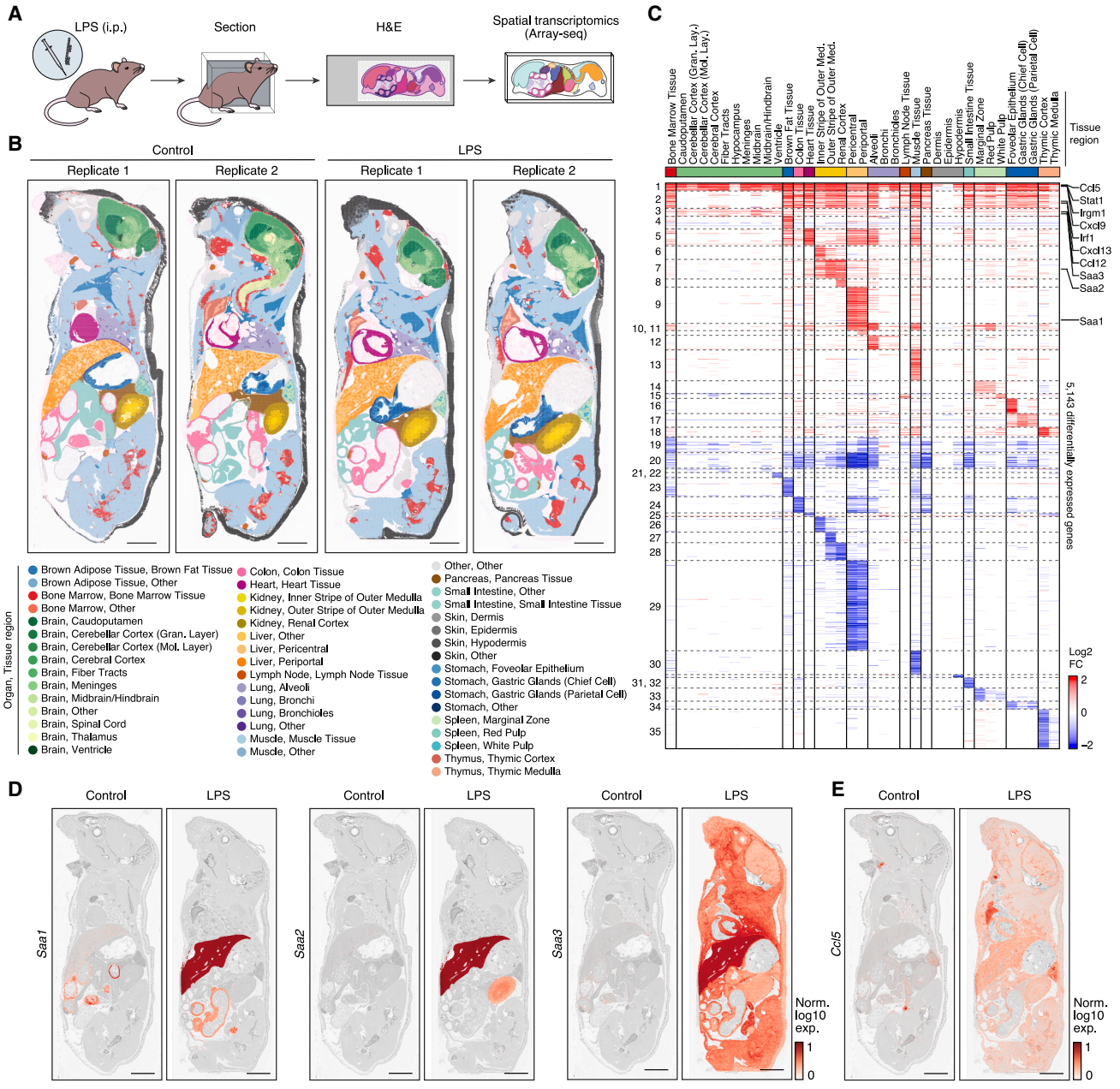

Figure 4. Spatiomolecular mapping of systemic inflammation upon endotoxemia

(A) Schematic overview of the experimental workflow.

(B) Spatial annotation of tissue regions across 16 main organ systems in our whole-mouse sections from mice at 12 h post-sublethal LPS injection (LPS) or untreated controls (control).

(C) Heatmap of differentially expressed genes (rows) from spatial transcriptomic mRNA profiles ordered by *k*-means clustering (numbers on the left, horizontal dashed lines) and organs and their subregions (columns; colors indicating main organ types). Values are $\log_2$ fold-changes in LPS relative to matching control tissue regions (false discovery rate (FDR)-adjusted p value < 0.01, Wilcoxon rank-sum test with Benjamini-Hochberg correction).

(D and E) Spatial expression of indicated genes overlaid on grayscale H&E images from whole-mouse sections from control and LPS-treated mice.

Scale bars: 5 mm (B, D, and E).

Gran, granular; Mol, molecular; Norm, normalized; Exp, expression.

See also Figure S6 and Tables S3 and S4.

Please cite this article in press as: Clevenger et al., Whole-body molecular and cellular mapping of the laboratory mouse, Cell (2026), https://doi.org/10.1016/j.cell.2026.03.006

CellPress

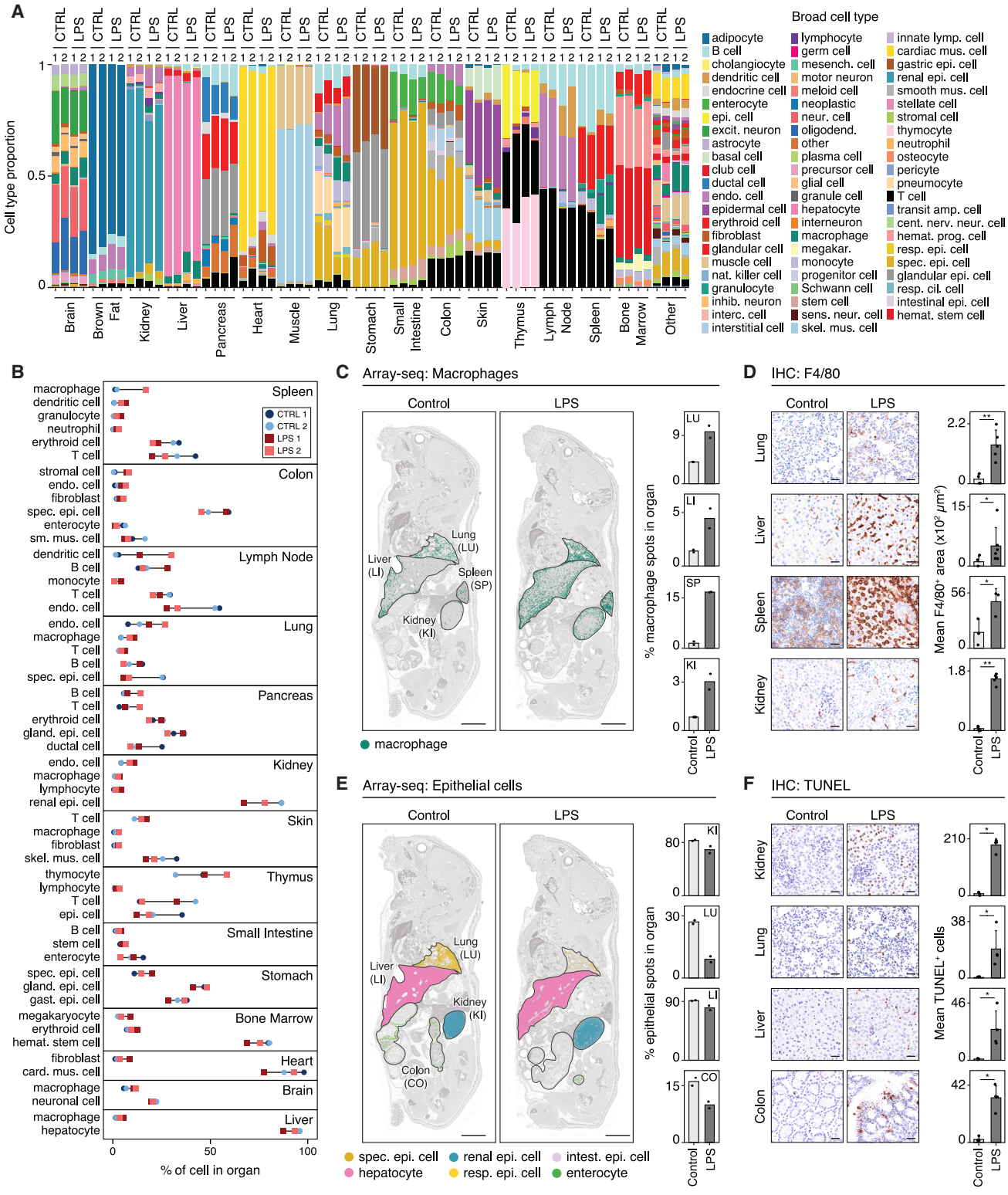

Figure 5. Body-wide changes in cell-type proportions in endotoxemia

(A) Stacked bar plot showing the proportion of indicated broad cell types (colors) across indicated organs (bottom) in whole-mouse Array-seq data from two independent mice (1 and 2, top) at 12 h post-sublethal LPS injection (LPS) or untreated controls (Control).

(legend continued on next page)

Please cite this article in press as: Clevenger et al., Whole-body molecular and cellular mapping of the laboratory mouse, Cell (2026), https://doi.org/10.1016/j.cell.2026.03.006

changes in myeloid cell recruitment and migration across tissues.[37–39]

Our whole-mouse spatial profiles thus revealed both local and systemic transcriptional responses to LPS and intercellular signaling programs mediating tissue responses to systemic inflammation.

Body-wide changes in cellular composition during endotoxemia

We quantified changes in the composition and distribution of cell types in our whole-mouse section profiles from control and LPS-treated mice (STAR Methods). The tissue-level compositions and distributions of cell types were broadly similar across control and LPS sections, although differences could be detected across most, if not all, tissues (Figures 5A and 5B). For example, immune cell types varied across the body in response to LPS, including a multi-tissue increase in macrophages in the lung, liver, spleen, and kidney, as validated by immunohistochemistry (Figures 5C and 5D), which supported the established role of macrophages in mediating the systemic response to LPS.[40] Lung and splenic neutrophils increased upon LPS treatment, as validated by immunohistochemistry (Figures S7A and S7B), as well as mast cells across several tissues (Figure S7C), which can perhaps be linked to the negative effects of these cells in tissue injury.[41] Conversely, splenic lymphocytes and thymocytes decreased markedly during endotoxemia, as confirmed by TUNEL staining and in agreement with the known effects of endotoxemia on these cell types (Figures S7D and S7E).[42,43] Non-hematopoietic cell types also displayed significant changes across tissues, including altered endothelial, fibroblast, and epithelial cell-type proportions in lungs, kidney, liver, or heart, as validated in part using TUNEL staining, in agreement with previous reports on endotoxemia-driven apoptosis in these tissues, and vimentin (Figures 5E and 5F; Figures S7F and S7G).[44–47]

Overall, our spatial data enabled cross-tissue comparisons across whole-body sections, revealing body-wide changes in the distribution of cell types in endotoxemia.

Cell-type-specific transcriptional responses to endotoxemia

We measured gene expression changes upon LPS treatment in 61 broad cell types distributed across 37 tissue subregions from 16 organs. First, we collapsed the total numbers of differentially expressed genes in response to LPS across the 61 broad cell types into 15 core cell types across 16 organs, revealing that non-hematopoietic cells drive most changes across organs (Figure 6A). For example, epithelial cells in liver (64.49%), kidney (67.06%), stomach (78.95%), small intestine (57.13%), and colon (43.03%) accounted for the majority of LPS-induced transcriptional changes, followed by muscle cells in heart (74.2%), skin (46.93%), and skeletal muscle (76.77%) (Figure 6A; STAR Methods). Blood and immune cell types showed the greatest changes in transcriptional states in lymphoid tissues (spleen, thymus, bone marrow) and in lung and liver (Figure 6A). Second, we found that out of the 57 broad cell types examined, macrophages, endothelial cells, and fibroblasts showed significant changes in transcriptional states in response to LPS across the most tissues (Figure 6B), including 68.3% (28/41) of tissues for macrophages, 58.5% (24/41) for fibroblasts, and 53.6% (22/41) for endothelia (Table S5A). Therefore, macrophages not only increased in numbers across organs upon LPS but also modified their transcriptional states in tissue-specific ways (Figures 5C, 5D, and 6B). Lastly, at the gene level, LPS triggered gene expression changes that were shared or cell-type-specific across tissues (Table S5B). For example, epithelial and immune cells displayed substantial overlap in differentially expressed genes upon LPS, reflecting changes in IL-17A (FDR = 1.99×10^{-11}), type II interferon (FDR = 2.89×10^{-8}), and IL-1 (FDR = 2.08×10^{-5}) signaling pathways. Moreover, epithelial cells in the lung, kidney, colon, skin, or thymus exhibited tissue-specific changes in gene expression upon LPS, likely reflecting specialized gene programs present across different epithelia (Table S5B).

Our results suggested that while LPS triggers both common and unique gene expression programs across cell types, the magnitude, specificity, and directionality of these transcriptional responses are shaped by both cell identity and tissue context.

STAT1 and IRF1 coordinate body-wide responses to LPS

We studied the multi-tissue regulation of ISGs across all tissues and cell types detected. We focused on transcription factors STAT1 and IRF1 because: (1) they were both widely upregulated across tissues albeit with some differences in tissue specificities (Figures 7A and 7B), in agreement with our previously reported bulk, whole-tissue RNA-seq data upon LPS (Figure 7C)[28]; (2) they were predicted computationally to regulate the ISGs altered in our bulk tissue LPS data (Figure 7D); and (3) while they are known regulators of ISGs,[48] their target genes have not been systematically mapped across tissues and cell types. To functionally test STAT1 and IRF1 in endotoxemia, we injected a

(B) Line plot showing the proportion of significantly altered broad cell types (Propeller test with arcsine transformation; FDR < 0.2) across organs in whole-mouse Array-seq datasets from LPS ($n = 2$) or control (CTRL; $n = 2$) mice.

(C and E) Spatial distribution of indicated cell-type signatures (colors) overlaid on grayscale H&E images from whole-mouse sections from control and LPS-treated mice for indicated organs (black line contours). Bar plots indicate the proportions of each cell-type signature in the indicated organs for control and LPS conditions.

(D and F) Images from immunohistochemistry (IHC) analysis of F4/80 (D) and TUNEL (F) staining for the indicated organs (rows). Bar plots show quantifications of the mean positive IHC signal area per field for each biological replicate ($n = 3$–5 independent mice).

Statistical comparisons between LPS-treated and control groups for all immunohistochemistry quantifications used a one-sided Mann-Whitney U test. *$p < 0.05$, **$p < 0.01$. Scale bars: 5 mm (C and E); 25 μm (D and F). Error bars, SD (D and F).

Endo, endothelial; Spec, specialized; Epi, epithelial; Sm, smooth; Mus, muscle; Gland, glandular; Skel, skeletal; Gast, gastric; Hemat, hematopoietic; Card, cardiac; Resp, respiratory; Intest, intestinal; Nat, natural; Inhib, inhibitory; Interc, intercalated; Neur, neuronal; Oligodend, oligodendrocyte; Sens, sensory; Megakar, megakaryocyte; Lymp, lymphocyte; Amp, amplifying; Cent, central; Nerv, nervous; Cil, ciliated.

See also Figure S7.

Please cite this article in press as: Clevenger et al., Whole-body molecular and cellular mapping of the laboratory mouse, Cell (2026), https://doi.org/10.1016/j.cell.2026.03.006

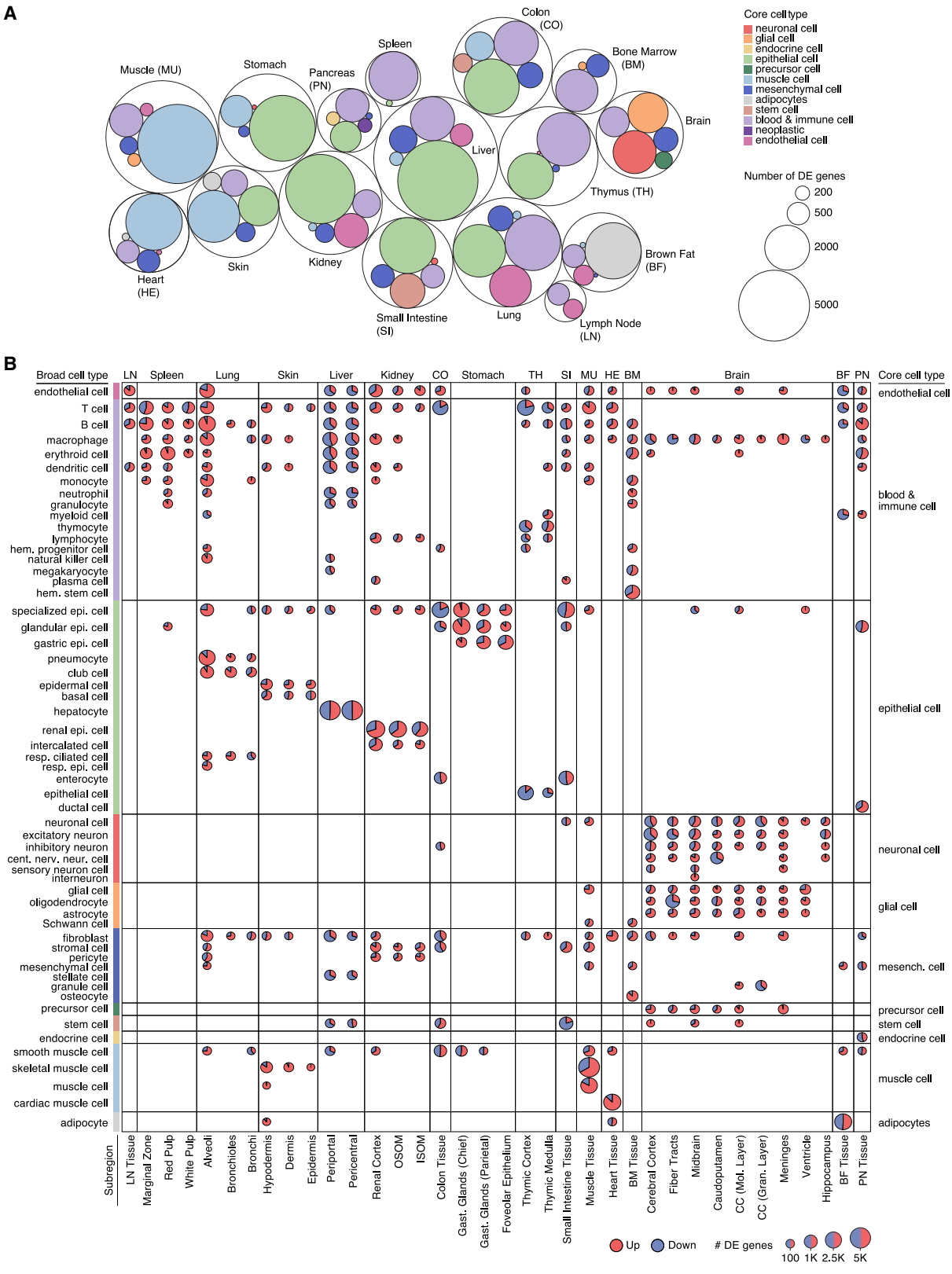

(legend on next page)

Please cite this article in press as: Clevenger et al., Whole-body molecular and cellular mapping of the laboratory mouse, Cell (2026), https://doi.org/10.1016/j.cell.2026.03.006

sublethal dose of LPS into *Irf1*$^{-/-}$ and *Stat1*$^{-/-}$ mice. We found that both knockout mice abrogated the decrease in body temperature seen in wild-type mice after LPS injection (Figure 7E), in agreement with previous work.[49,50] Moreover, *Irf1*$^{-/-}$ and *Stat1*$^{-/-}$ mice reverted the organism-wide ISG response driven by LPS in our whole-tissue RNA-seq data (Figures 7F–7H; Table S6). While the LPS-induced genes regulated by STAT1 and IRF1 across organs overlapped for the most part, tissue-specific effects were also observed, as in liver, kidney, and lung (Figure 7I).

Next, we investigated the cell types in which STAT1 and IRF1, as well as STAT1- and IRF1-dependent genes, were differentially expressed across our whole-mouse sections. We found that both *Stat1* and *Irf1* were upregulated in response to LPS across nearly all hematopoietic and non-hematopoietic cell types, including epithelia, endothelia, fibroblasts, muscle, and neurons, across the 16 organs tested (Figure 7F; Figure S12D). In total, we found that 57.3% (43/75) of the broad cell types defined across all tissues showed a >1.5-fold increase (FDR < 0.05) in *Stat1* and/or *Irf1* expression (Figure S12D). One of the most prominent differences between *Stat1* and *Irf1* expression upon LPS was that *Stat1* was significantly upregulated in brain cell types, whereas *Irf1* was not (Figure S12D). Moreover, we used our whole-tissue RNA-seq profiles from LPS-treated *Irf1*$^{-/-}$, *Stat1*$^{-/-}$, and wild-type mice to define organ-specific gene signatures that were positively or negatively regulated by STAT1 or IRF1 upon LPS treatment (STAR Methods). We found that changes in STAT1- and IRF1-dependent gene signatures largely mirrored *Stat1* and *Irf1* expression across 48 broad cell types tested in 7 organs (Figure 7F), supporting cell-intrinsic roles for both transcription factors in regulating ISGs across the body.

Lastly, we systematically mapped the gene regulatory networks controlled by STAT1 and IRF1 across cell types and tissues in our whole-mouse profiles (STAR Methods). We identified 40 IRF1-specific regulons, 39 STAT1-specific regulons, and 19 shared regulons across all 16 organs and 9 core cell types tested (Figure S8A; Table S7A). IRF1 and STAT1 regulons upregulated by LPS were found in most tissues except brown fat, thymus, and gut, which exhibited downregulated regulons (Figure S8A). Moreover, IRF1 and STAT1 were similarly active across most tissues except for skin (STAT1 dominant) and brain (IRF1 dominant) (Figure S8A). Next, we compared IRF1 and STAT1 regulons (1) across core cell types for each organ (Figures S8B–S8F), and (2) across organs for each core cell type (Figures S8G and S8H; Table S7B). We found that IRF1-specific, STAT1-specific, and shared regulons were collectively cell-type specific within an organ type and organ-specific for a given cell type (Figures S8B–S8H). Among the IRF1-specific, STAT1-specific, and shared regulon genes upregulated by LPS, ISGs formed a substantial fraction of the response (immune cells: 37.5%, epithelial cells: 34.5%) (Figures S8G and S8H). Moreover, IRF1- and STAT1-controlled genes associated with similar pathways across tissues and cell types, including antigen presentation, oxidative stress, and type II interferon, IL-17A, and IL-1 signaling, (Figures S8B–S8H), suggesting that different gene regulatory network structures (e.g., IRF1-specific in cell type A of tissue A or STAT1-specific in cell type B of tissue B) can control similar biological outcomes for tissue responses to endotoxemia.

Taken together, our results demonstrate that body-wide spatiomolecular profiling enables the quantitative analysis of gene regulation in response to disease, such as systemic inflammation, and the effects of genetic perturbations across cell types within their native tissue environments.

DISCUSSION

The laboratory mouse is a central model system for the study of mammalian biology in basic and clinical sciences. However, studies of homeostasis and disease mechanisms in mice have largely remained confined to tissue-by-tissue, cell-by-cell approaches because we lack technologies for body-wide phenotyping of mice at the molecular and cellular levels. Here, we created tools that enable body-wide spatiomolecular profiling of mice by combining whole-mouse sectioning and Array-seq, a large-format spatial transcriptomics platform.[10] We used 10-μm-thick, whole-body sections from healthy 6-week-old mice to obtain spatiotranscriptomics data covering 5 million nuclei per section. We exploited our whole-mouse spatiomolecular profiles to create an artificial intelligence framework, LABEL, for pan-body annotation of organs, tissues, and cell types from H&E-stained images. Lastly, we applied our whole-mouse profiling approach to a mouse model of endotoxemia, revealing the spatiomolecular and spatiocellular effects of systemic inflammation on the body. Taken together, our work established experimental and computational resources for the whole-body spatiomolecular profiling of laboratory mice, paving the way for body-wide studies of mouse models and other organisms across conditions.

What may be the use of whole-mouse spatial profiling for biomedical research fields using the laboratory mouse and beyond? Our work demonstrated the power of spatiomolecular profiling tools bridging the molecular, cellular, tissue, and whole-body scales to reveal the detailed makeup of the mouse

Figure 6. Cell-type- and tissue-specific transcriptional responses to systemic inflammation

(A) Circle packing plot of differentially expressed (DE; FDR < 0.05, $|\log_2$ fold change$| > 0.25$, Wilcoxon rank-sum test with Benjamini-Hochberg correction) gene counts (circle size) between LPS-treated and control mice across the indicated 12 core cell types (inner circles, colors) and 16 organs (outer circles). The top 5 core cell types are shown per organ.

(B) Dot plot with pie charts showing DE gene counts (dot size) for broad cell types (rows) across tissue regions of annotated organs (columns) calculated between LPS-treated and control mice (FDR < 0.05, $|\log_2$ fold change$| > 0.25$). Pie segments indicate the proportion of upregulated (red) or downregulated (blue) genes. LN, lymph node; SI, small intestine; BM, bone marrow; B, brown; PN, pancreas; OSOM, outer stripe of outer medulla; ISOM, inner stripe of outer medulla; Gast, gastric; CC, cerebellar cortex; Mol, molecular; Gran, granular; Hem, hematopoietic; Prog, progenitor; Epi, epithelial; Resp, respiratory; Cent, central; Nerv, nervous; Neur, neuronal.

See also Table S5.

Please cite this article in press as: Clevenger et al., Whole-body molecular and cellular mapping of the laboratory mouse, Cell (2026), https://doi.org/10.1016/j.cell.2026.03.006

CellPress

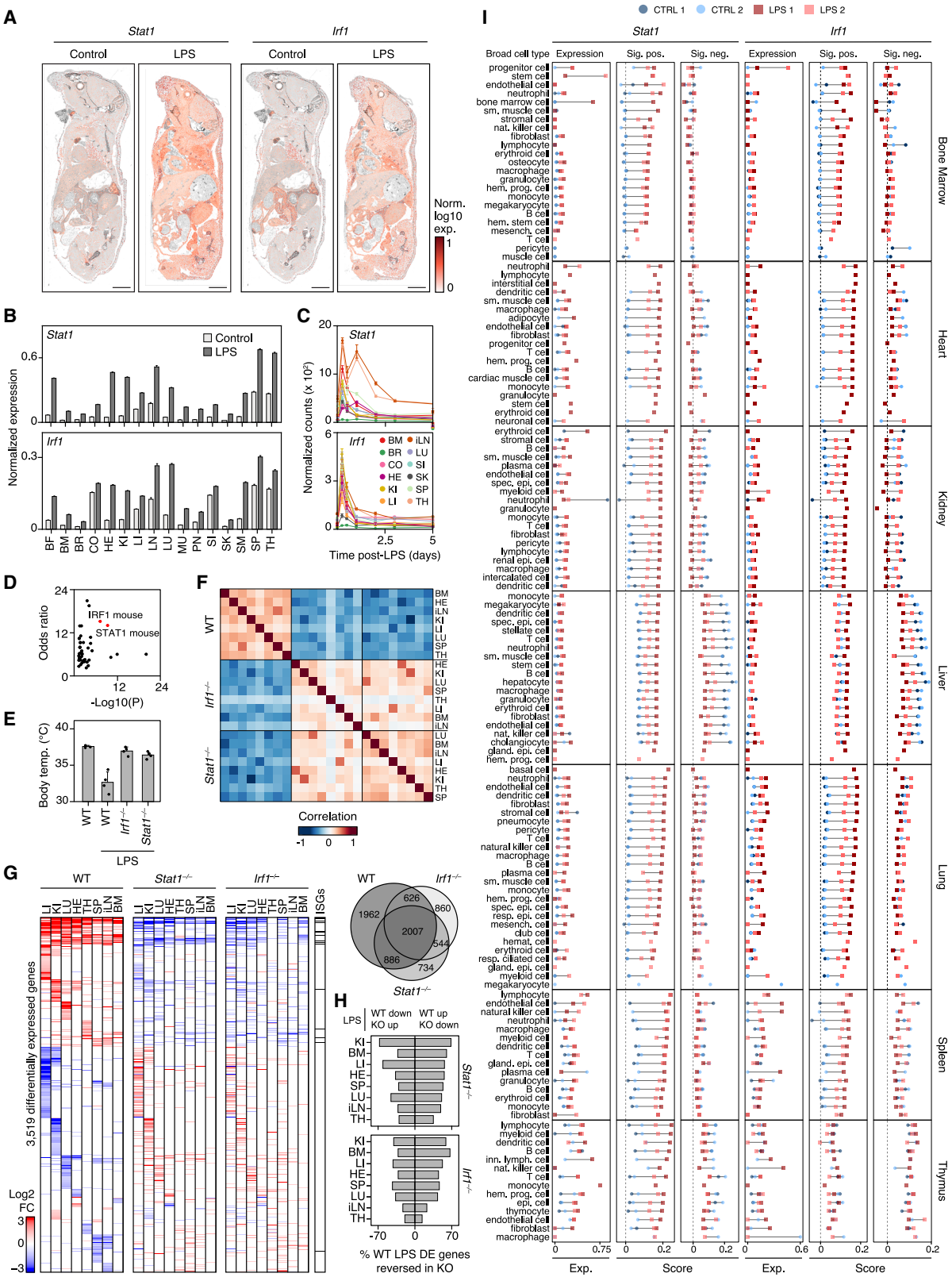

(legend on next page)

Please cite this article in press as: Clevenger et al., Whole-body molecular and cellular mapping of the laboratory mouse, Cell (2026), https://doi.org/10.1016/j.cell.2026.03.006

body and its changes during systemic inflammation. Moving beyond these proof-of-principle experiments, we foresee many applications for our body-wide profiling tools to study biological processes in any field of inquiry that relies on mouse models. First, we anticipate that whole-mouse section profiling will yield fundamental knowledge about the effects of genetic mutations or variations on the organismal phenotype of mice. For example, a critical bottleneck in mouse genetics is the phenotyping of each mutant.[51] Our work will enable the detailed characterization of the effects of genetic changes on all cell types and tissues of the mouse body at once. Results from such body-wide genotype-to-phenotype mapping efforts will yield critical insights to deepen our understanding of the organismal biology of the mouse and mammalian organisms.

Second, the spatiomolecular profiles of whole-mouse sections yield high-resolution information about the spatial arrangement and the states of cell types across all organ systems of the body. Mining these whole-mouse maps of cell states and interactions will help to decipher the emerging properties of cell-cell interactions across tissues and how these properties change in disease. Third, we predict that whole-mouse profiles will be beneficial for organismal pharmacology and toxicology studies and inform drug target discovery. For example, using whole-mouse profiling to probe the effects of existing and candidate drugs, such as small molecules, biologics, or cells, will produce critical information about the desired and undesired effects of drugs across all the cells and tissues of the body. Moreover, combining data whole-mouse spatial transcriptomics and drug biodistribution will refine our understanding of drug mechanisms of action across targeted tissues. Fourth, our work will help profile the whole bodies of other mammalian and non-mammalian species as well as whole organs from mammals larger than mice, because Array-seq is readily transferable to other laboratories, uses commercially available reagents, and is cost-effective, making body- or organ-wide profiling accessible and scalable.[10]

Lastly, we used our whole-mouse spatial transcriptomics data to build a machine learning model, LABEL, to automatically annotate organs, tissues, and cell types on images from H&E-stained sections. The broad applicability of LABEL for basic and pre-clinical studies in mice will help to propel (1) phenotyping workflows prior to in-depth analyses with staining and sequencing, or (2) large-scale spatial annotation efforts, when sequencing is impractical or cost-prohibitive. In the future, we envision that similar models can be readily trained across mammalian and non-mammalian species using matched histological and spatiomolecular data, which will enable the virtual staining of tissues and cells at scale and fuel basic research across species and model systems. Moreover, we predict that building a histological foundation model of the laboratory mouse from body-wide H&E images in 3D will improve our computational framework to annotate histology images. Lastly, extending LABEL capabilities to human H&E data will benefit existing clinical pathology workflows by informing diagnosis and therapy decisions for individual patients.

Overall, our study reported a unified experimental and computational framework for body-wide studies of the laboratory mouse, providing a paradigm shift in phenotyping mouse models and a roadmap for similar efforts across model and non-model organisms and clinical samples.

Limitations of the study

First, whole-mouse sectioning requires a specialized instrument, a cryomacrotome, to obtain sagittal sections of 6-week-old C57BL/6J mice (~2 × 6 cm in surface area; STAR Methods). Although younger, smaller animals can be sectioned using readily available standard cryomicrotomes across institutions.

Figure 7. IRF1 and STAT1 impact body-wide transcriptional responses to LPS

(A) Spatial expression of *Stat1* (left) and *Irf1* (right) overlaid on grayscale H&E images from whole-mouse Array-seq data from LPS-treated and control mice. Scale bars: 5 mm.

(B) Mean normalized $\log_{10}$ expression (*y* axis) of *Stat1* (top) and *Irf1* (bottom) across all Array-seq spots covering indicated organs (*x* axis) from the whole-mouse section data of LPS-treated and control mice. Error bars, SEM.

(C) Normalized counts for indicated genes and organs (color) from mice injected with a sublethal dose of LPS and collected at indicated time points prior to whole-tissue, bulk RNA-seq (n = 2–4 independent mice). Error bars, SEM.

(D) Transcription factor enrichment analysis (STAR Methods) on LPS-regulated genes identified from bulk RNA-seq (n = 2–4 independent mice).

(E) Measurements of rectal temperature in mice of the indicated genotypes at 12 h post-sublethal LPS injection (LPS) or without LPS treatment in control, wild-type mice. Error bars, SEM.

(F) Heatmap of correlation (Pearson's coefficient) between bulk, whole-tissue RNA-seq profiles from indicated organs and genotypes following LPS treatment.

(G) Heatmap of differentially expressed (DE) genes (rows) from whole-tissue RNA-seq profiles ordered by k-means clustering and organ type (top). Data are shown for wild-type mice at 12 h post-sublethal LPS injection (left) and for *Stat1*$^{-/-}$ (center) and *Irf1*$^{-/-}$ (right) mice at 16 h post-LPS injection. Values are $\log_2$ fold changes relative to matching untreated controls for wild-type (FDR < 0.01, |fold change| > 2; n = 4 independent mice) and relative to LPS-treated wild-type for knockouts (FDR < 0.05 using moderated *t* test with Benjamini-Hochberg correction, |fold change| > 2; n = 2–4 independent mice per group). Interferon-stimulated genes (ISGs) are indicated in black on the right side of the heatmaps. The Venn diagram (top right) indicates the overlap in DE genes between all three genotypes across all 8 organs measured.

(H) Percentage (*x* axis) of LPS-regulated genes shown in (G) per indicated organs (*y* axis) for which differential expression (DE) is opposite in direction in wild-type (WT) versus indicated knockout (KO) mouse strains at 16 h post-sublethal LPS injection.

(I) Mean normalized log10 expression (exp.) of *Stat1* and *Irf1* and module scores (score) for gene sets positively or negatively regulated by IRF1 or STAT1 in response to LPS (defined using bulk RNA-seq shown in E) across indicated organs (colors) and broad cell types (rows) from our whole-mouse Array-seq datasets. Norm, normalized; Exp., expression; BF, brown fat; BM, bone marrow; BR, brain; CO, colon; HE, heart; KI, kidney; LI, liver; LN, lymph node; LU, lung; MU, muscle; PN, pancreas; SI, small intestine; SK, skin; SM, stomach; SP, spleen; TH, thymus; iLN, inguinal lymph node; Hem, hematopoietic; Spec, specialized; Gland, glandular; Resp, respiratory; Sm, smooth; Mesench, mesenchymal; Nat, natural; Epi, epithelial; Prog, progenitor; Inn, innate; FC, fold-change; DE, differentially expressed; WT, wild-type.

See also Figure S8 and Tables S6 and S7.

Second, optimizing the Array-seq slide design and the conditions of whole-mouse section permeabilization, RNA capture, and *in situ* reverse transcription, as well as the use of targeted RNA-seq approaches, will further improve the accuracy and depth of gene expression measurements while reducing costs. Third, while our method does not achieve single-cell-level spatial resolution, specimen expansion techniques applied pre- or post-sectioning will help address this limitation. Lastly, our LABEL model was trained on data from four female C57BL6/J mice profiled in a single sagittal plane, thereby limiting coverage of the full histological heterogeneity found in the mouse body across varying biological conditions. Future work generating whole-mouse profiles at higher resolution and encompassing all types of mouse tissues and cells across a broader array of conditions (e.g., age, sex, genetics, diseases, microbiota, etc.) will enhance the power, resolution, and applicability of our LABEL annotation model and fuel the development of additional artificial intelligence models useful to study the mouse and other mammalian organisms.

RESOURCE AVAILABILITY

Lead contact

Requests for further information and resources should be directed to and will be fulfilled by the lead contact, Nicolas Chevrier (nchevrier@uchicago.edu).

Materials availability

This study did not generate unique reagents.

Data and code availability

Sequencing data analyzed in this study have previously been deposited in the Gene Expression Omnibus under GEO: GSE266246, GSE248904. Analysis scripts and preprocessed datasets are publicly available at Zenodo: https://doi.org/10.5281/zenodo.15741906 and GitHub: https://github.com/chevrierlab/WMST-paper. Code for the LABEL computational pipeline for the virtual staining of whole-mouse section H&E imaging data is available as a compute capsule at Code Ocean: https://doi.org/10.24433/CO.3645054.v1.

ACKNOWLEDGMENTS

We thank Marc Jenkins and colleagues for inspiring this work (PMID: 11242050); Chevrier lab members for valuable discussions; the University of Chicago core facilities, including the Single Cell Immunophenotyping Core (SCR_025140), Animal Resources Center, Research Computing Center, Integrated Light Microscopy Core, and Human Tissue Resource Center, for technical support; and SciStories for assistance with artwork. D.C. was supported by NIH T32-GM00728. M.T. was supported by the Astellas Foundation for Research on Metabolic Disorders. F.B. was supported by the National Natural Science Foundation of China (grant no. 62573131), the Shanghai Committee of Science and Technology (grant no. 25JS2810300), the Fudan Kunpeng & Ascend Center of Cultivation, and the Xiaomi Young Scholar Award. N.C. was supported by NIH DP2-AI145100, U01-AI160418, R33-CA297902, P30-DK042086, and P30-DK020595; CZI grant DAF2020-217464 and grant https://doi.org/10.37921/767230ofotux from the Chan Zuckerberg Initiative DAF, an advised fund of the Silicon Valley Communicaty Foundation (funder: https://doi.org/10.13039/100014989); the University of Chicago AI Initiative and the Physics Frontier Center for Living Systems funded by the National Science Foundation (PHY-2317138); Agilent ACT-UR program awards (#4843, #5100); the UChicago Comprehensive Cancer Center Janet D. Rowley Discovery Fund; the Duckworth Family Commercial Promise Cancer Research Award; the Robert Lavichant Faculty Innovation Award; and the UChicago Pritzker School of Molecular Engineering.

AUTHOR CONTRIBUTIONS

N.C. conceptualized the study. M.H.C., D.C., A.P., and M.T. performed data analyses. D.C. generated the whole-mouse spatial transcriptomics data. A.P. created the spatial cell-type assignment pipeline. B.L. and F.B. built the machine learning algorithm, LABEL, for H&E annotation. M.T. analyzed *Irf1* and *Stat1* KO mice with help from M.P. and G.R. T.K. provided technical expertise for whole-mouse sectioning. L.M. performed immunohistochemistry analyses. M.H.C. and N.C. wrote the manuscript with input from all authors. N.C. supervised the project.

DECLARATION OF INTERESTS

D.C. and N.C. are authors on patent PCT/US23/13010 covering the Array-seq technology. A.P. is the founder and CEO of Combinatics.

STAR★METHODS

Detailed methods are provided in the online version of this paper and include the following:

- KEY RESOURCES TABLE
- EXPERIMENTAL MODEL AND STUDY PARTICIPANT DETAILS
  - Mice
- METHOD DETAILS
  - Mouse lipopolysaccharide injections
  - Custom oligonucleotide microarray design for Array-seq slides
  - Array-seq slide preparation
  - Whole-mouse histological sectioning
  - Whole-mouse H&E staining and imaging
  - Whole-mouse section permeabilization and reverse transcription for Array-seq
  - Array-seq library preparation and sequencing
  - Mouse tissue harvest for for whole-tissue RNA-seq
  - Whole-tissue RNA extraction
  - Whole-tissue RNA sequencing
  - Immunohistochemistry
- QUANTIFICATION AND STATISTICAL ANALYSIS
  - Bulk mouse tissue RNA sequencing data analysis
  - Differential expression and pathway analysis
  - Whole-mouse spatial transcriptomics data analysis
  - LABEL algorithm for the virtual staining of histology H&E images
  - Immunohistochemistry image data analysis

SUPPLEMENTAL INFORMATION

Supplemental information can be found online at https://doi.org/10.1016/j.cell.2026.03.006.

Received: June 27, 2025
Revised: December 15, 2025
Accepted: March 5, 2026

REFERENCES

1. Southern, P.J., Blount, P., and Oldstone, M.B. (1984). Analysis of persistent virus infections by in situ hybridization to whole-mouse sections. Nature *312*, 555–558. https://doi.org/10.1038/312555a0.
2. Reinhardt, R.L., Khoruts, A., Merica, R., Zell, T., and Jenkins, M.K. (2001). Visualizing the generation of memory CD4 T cells in the whole body. Nature *410*, 101–105. https://doi.org/10.1038/35065111.
3. Yang, B., Treweek, J.B., Kulkarni, R.P., Deverman, B.E., Chen, C.K., Lubeck, E., Shah, S., Cai, L., and Gradinaru, V. (2014). Single-cell phenotyping within transparent intact tissue through whole-body clearing. Cell *158*, 945–958. https://doi.org/10.1016/j.cell.2014.07.017.

4. Tainaka, K., Kubota, S.I., Suyama, T.Q., Susaki, E.A., Perrin, D., Ukai-Tadenuma, M., Ukai, H., and Ueda, H.R. (2014). Whole-body imaging with single-cell resolution by tissue decolorization. Cell *159*, 911–924. https://doi.org/10.1016/j.cell.2014.10.034.

5. Kubota, S.I., Takahashi, K., Nishida, J., Morishita, Y., Ehata, S., Tainaka, K., Miyazono, K., and Ueda, H.R. (2017). Whole-Body Profiling of Cancer Metastasis with Single-Cell Resolution. Cell Rep. *20*, 236–250. https://doi.org/10.1016/j.celrep.2017.06.010.

6. Cai, R., Pan, C., Ghasemigharagoz, A., Todorov, M.I., Förstera, B., Zhao, S., Bhatia, H.S., Parra-Damas, A., Mrowka, L., Theodorou, D., et al. (2019). Panoptic imaging of transparent mice reveals whole-body neuronal projections and skull-meninges connections. Nat. Neurosci. *22*, 317–327. https://doi.org/10.1038/s41593-018-0301-3.

7. Mai, H., Luo, J., Hoeher, L., Al-Maskari, R., Horvath, I., Chen, Y., Kofler, F., Piraud, M., Paetzold, J.C., Modamio, J., et al. (2024). Whole-body cellular mapping in mouse using standard IgG antibodies. Nat. Biotechnol. *42*, 617–627. https://doi.org/10.1038/s41587-023-01846-0.

8. Liu, L., Chen, A., Li, Y., Mulder, J., Heyn, H., and Xu, X. (2024). Spatiotemporal omics for biology and medicine. Cell *187*, 4488–4519. https://doi.org/10.1016/j.cell.2024.07.040.

9. Moses, L., and Pachter, L. (2022). Museum of spatial transcriptomics. Nat. Methods *19*, 534–546. https://doi.org/10.1038/s41592-022-01409-2.

10. Cipurko, D., Ueda, T., Mei, L., and Chevrier, N. (2024). Repurposing large-format microarrays for scalable spatial transcriptomics. Nat. Methods *22*, 145–155. https://doi.org/10.1038/s41592-024-02501-5.

11. Chen, R.J., Ding, T., Lu, M.Y., Williamson, D.F.K., Jaume, G., Song, A.H., Chen, B., Zhang, A., Shao, D., Shaban, M., et al. (2024). Towards a general-purpose foundation model for computational pathology. Nat. Med. *30*, 850–862. https://doi.org/10.1038/s41591-024-02857-3.

12. Mukherjee, P., Roy, S., Ghosh, D., and Nandi, S.K. (2022). Role of animal models in biomedical research: a review. Lab. Anim. Res. *38*, 18. https://doi.org/10.1186/s42826-022-00128-1.

13. Kawamoto, T., and Kawamoto, K. (2021). Preparation of Thin Frozen Sections from Nonfixed and Undecalcified Hard Tissues Using Kawamoto's Film Method (2020). Methods Mol. Biol. *2230*, 259–281. https://doi.org/10.1007/978-1-0716-1028-2_15.

14. Kawamoto, T., and Kawamoto, K. (2014). Preparation of thin frozen sections from nonfixed and undecalcified hard tissues using Kawamot's film method (2012). Methods Mol. Biol. *1130*, 149–164. https://doi.org/10.1007/978-1-62703-989-5_11.

15. Kawamoto, T. (2003). Use of a new adhesive film for the preparation of multi-purpose fresh-frozen sections from hard tissues, whole-animals, insects and plants. Arch. Histol. Cytol. *66*, 123–143. https://doi.org/10.1679/aohc.66.123.

16. Sunkin, S.M., Ng, L., Lau, C., Dolbeare, T., Gilbert, T.L., Thompson, C.L., Hawrylycz, M., and Dang, C. (2013). Allen Brain Atlas: an integrated spatio-temporal portal for exploring the central nervous system. Nucleic Acids Res. *41*, D996–D1008. https://doi.org/10.1093/nar/gks1042.

17. Sáenz, J.B., and Mills, J.C. (2018). Acid and the basis for cellular plasticity and reprogramming in gastric repair and cancer. Nat. Rev. Gastroenterol. Hepatol. *15*, 257–273. https://doi.org/10.1038/nrgastro.2018.5.

18. Ben-Moshe, S., and Itzkovitz, S. (2019). Spatial heterogeneity in the mammalian liver. Nat. Rev. Gastroenterol. Hepatol. *16*, 395–410. https://doi.org/10.1038/s41575-019-0134-x.

19. Patil, A., and Patil, A. (2022). CellKb Immune: a manually curated database of mammalian hematopoietic marker gene sets for rapid cell type identification. Preprint at bioRxiv. https://doi.org/10.1101/2020.12.01.389890.

20. Cable, D.M., Murray, E., Zou, L.S., Goeva, A., Macosko, E.Z., Chen, F., and Irizarry, R.A. (2022). Robust decomposition of cell type mixtures in spatial transcriptomics. Nat. Biotechnol. *40*, 517–526. https://doi.org/10.1038/s41587-021-00830-w.

21. Kleshchevnikov, V., Shmatko, A., Dann, E., Aivazidis, A., King, H.W., Li, T., Elmentaite, R., Lomakin, A., Kedlian, V., Gayoso, A., et al. (2022). Cell2location maps fine-grained cell types in spatial transcriptomics. Nat. Biotechnol. *40*, 661–671. https://doi.org/10.1038/s41587-021-01139-4.

22. Ma, Y., and Zhou, X. (2022). Spatially informed cell-type deconvolution for spatial transcriptomics. Nat. Biotechnol. *40*, 1349–1359. https://doi.org/10.1038/s41587-022-01273-7.

23. Kim, J., Kwon, N., Chang, S., Kim, K.T., Lee, D., Kim, S., Yun, S.J., Hwang, D., Kim, J.W., Hwu, Y., et al. (2011). Altered branching patterns of Purkinje cells in mouse model for cortical development disorder. Sci. Rep. *1*, 122. https://doi.org/10.1038/srep00122.

24. Mason, P. (2011). Cerebellum. In Medical Neurobiology (Oxford University Press), pp. 537–558. https://doi.org/10.1093/med/9780195339970.003.0024.

25. Ashby, K.M., and Hogquist, K.A. (2024). A guide to thymic selection of T cells. Nat. Rev. Immunol. *24*, 103–117. https://doi.org/10.1038/s41577-023-00911-8.

26. Lancaster, J.N., Li, Y., and Ehrlich, L.I.R. (2018). Chemokine-Mediated Choreography of Thymocyte Development and Selection. Trends Immunol. *39*, 86–98. https://doi.org/10.1016/j.it.2017.10.007.

27. de Oliveira Neves, A.C., and Galván, I. (2020). Models for human porphyrias: Have animals in the wild been overlooked?: Some birds and mammals accumulate significant amounts of porphyrins in the body without showing the injurious symptoms observed in human porphyrias. BioEssays *42*, e2000155. https://doi.org/10.1002/bies.202000155.

28. Takahama, M., Patil, A., Richey, G., Cipurko, D., Johnson, K., Carbonetto, P., Plaster, M., Pandey, S., Cheronis, K., Ueda, T., et al. (2024). A pairwise cytokine code explains the organism-wide response to sepsis. Nat. Immunol. *25*, 226–239. https://doi.org/10.1038/s41590-023-01722-8.

29. Bafica, A., Feng, C.G., Santiago, H.C., Aliberti, J., Cheever, A., Thomas, K.E., Taylor, G.A., Vogel, S.N., and Sher, A. (2007). The IFN-inducible GTPase LRG47 (Irgm1) negatively regulates TLR4-triggered proinflammatory cytokine production and prevents endotoxemia. J. Immunol. *179*, 5514–5522. https://doi.org/10.4049/jimmunol.179.8.5514.

30. van der Poll, T., Shankar-Hari, M., and Wiersinga, W.J. (2021). The immunology of sepsis. Immunity *54*, 2450–2464. https://doi.org/10.1016/j.immuni.2021.10.012.

31. McBride, M.A., Patil, T.K., Bohannon, J.K., Hernandez, A., Sherwood, E.R., and Patil, N.K. (2020). Immune Checkpoints: Novel Therapeutic Targets to Attenuate Sepsis-Induced Immunosuppression. Front. Immunol. *11*, 624272. https://doi.org/10.3389/fimmu.2020.624272.

32. Kanamori, Y., Nita, A., Nakayama, K.I., Kurotaki, D., Harada, K., and Moroishi, T. (2025). Hepatocyte iron suppresses liver fibrosis via fibrolytic neutrophil recruitment in cholestasis. JHEP Rep. *7*, 101590. https://doi.org/10.1016/j.jhepr.2025.101590.

33. Reutershan, J., Morris, M.A., Burcin, T.L., Smith, D.F., Chang, D., Saprito, M.S., and Ley, K. (2006). Critical role of endothelial CXCR2 in LPS-induced neutrophil migration into the lung. J. Clin. Investig. *116*, 695–702. https://doi.org/10.1172/jci27009.

34. Mei, J., Liu, Y., Dai, N., Hoffmann, C., Hudock, K.M., Zhang, P., Guttentag, S.H., Kolls, J.K., Oliver, P.M., Bushman, F.D., et al. (2012). Cxcr2 and Cxcl5 regulate the IL-17/G-CSF axis and neutrophil homeostasis in mice. J. Clin. Investig. *122*, 974–986. https://doi.org/10.1172/jci60588.

35. Eash, K.J., Greenbaum, A.M., Gopalan, P.K., and Link, D.C. (2010). CXCR2 and CXCR4 antagonistically regulate neutrophil trafficking from murine bone marrow. J. Clin. Investig. *120*, 2423–2431. https://doi.org/10.1172/jci41649.

36. Hierholzer, C., Kelly, E., Lyons, V., Roedling, E., Davies, P., Billiar, T.R., and Tweardy, D.J. (1998). G-CSF instillation into rat lungs mediates neutrophil recruitment, pulmonary edema, and hypoxia. J. Leukoc. Biol. *63*, 169–174. https://doi.org/10.1002/jlb.63.2.169.

37. Kitade, H., Sawamoto, K., Nagashimada, M., Inoue, H., Yamamoto, Y., Sai, Y., Takamura, T., Yamamoto, H., Miyamoto, K., Ginsberg, H.N., et al. (2012). CCR5 plays a critical role in obesity-induced adipose tissue inflammation and insulin resistance by regulating both macrophage

recruitment and M1/M2 status. Diabetes *61*, 1680–1690. https://doi.org/10.2337/db11-1506.

38. Chavez, B., and Kiaris, H. (2025). Insights on the role of the chemokine CCL8 in pathology. Cell. Signal. *134*, 111951. https://doi.org/10.1016/j.cellsig.2025.111951.
39. Gröbner, S., Lukowski, R., Autenrieth, I.B., and Ruth, P. (2014). Lipopolysaccharide induces cell volume increase and migration of dendritic cells. Microbiol. Immunol. *58*, 61–67. https://doi.org/10.1111/1348-0421.12116.
40. Hoyer, F.F., Naxerova, K., Schloss, M.J., Hulsmans, M., Nair, A.V., Dutta, P., Calcagno, D.M., Herisson, F., Anzai, A., Sun, Y., et al. (2019). Tissue-Specific Macrophage Responses to Remote Injury Impact the Outcome of Subsequent Local Immune Challenge. Immunity *51*, 899–914.e7. https://doi.org/10.1016/j.immuni.2019.10.010.
41. Cai, C., Cao, Z., Loughran, P.A., Kim, S., Darwiche, S., Korff, S., and Billiar, T.R. (2011). Mast cells play a critical role in the systemic inflammatory response and end-organ injury resulting from trauma. J. Am. Coll. Surg. *213*, 604–615. https://doi.org/10.1016/j.jamcollsurg.2011.08.009.
42. Ayala, A., Herdon, C.D., Lehman, D.L., Ayala, C.A., and Chaudry, I.H. (1996). Differential induction of apoptosis in lymphoid tissues during sepsis: variation in onset, frequency, and the nature of the mediators. Blood *87*, 4261–4275. https://doi.org/10.1182/blood.V87.10.4261.bloodjournal87104261.
43. Lamkanfi, M., Moreira, L.O., Makena, P., Spierings, D.C.J., Boyd, K., Murray, P.J., Green, D.R., and Kanneganti, T.D. (2009). Caspase-7 deficiency protects from endotoxin-induced lymphocyte apoptosis and improves survival. Blood *113*, 2742–2745. https://doi.org/10.1182/blood-2008-09-178038.
44. Nakajima, Y., Mikami, O., Yoshioka, M., Arai, S., Miura, K., Koike, Y., Sato, M., Kobayashi, M., and Nakajima, E. (2000). Involvement of apoptosis in the endotoxemic lesions of the liver and kidneys of piglets. J. Vet. Med. Sci. *62*, 621–626. https://doi.org/10.1292/jvms.62.621.
45. Li, D., Liu, G., and Wu, Y. (2022). RORA alleviates LPS-induced apoptosis of renal epithelial cells by promoting PGC-1α transcription. Clin. Exp. Nephrol. *26*, 512–521. https://doi.org/10.1007/s10157-022-02184-2.
46. Li, X., Xiong, Q., Yang, Q., Shi, J., Han, Y., Dong, Y., Qian, J., Qian, Z., Wang, H., Wang, T., et al. (2024). PTPRO inhibits LPS-induced apoptosis in alveolar epithelial cells. Biochem. Biophys. Res. Commun. *718*, 150083. https://doi.org/10.1016/j.bbrc.2024.150083.
47. Nighot, M., Al-Sadi, R., Guo, S., Rawat, M., Nighot, P., Watterson, M.D., and Ma, T.Y. (2017). Lipopolysaccharide-Induced Increase in Intestinal Epithelial Tight Permeability Is Mediated by Toll-Like Receptor 4/Myeloid Differentiation Primary Response 88 (MyD88) Activation of Myosin Light Chain Kinase Expression. Am. J. Pathol. *187*, 2698–2710. https://doi.org/10.1016/j.ajpath.2017.08.005.
48. Sadler, A.J., and Williams, B.R.G. (2008). Interferon-inducible antiviral effectors. Nat. Rev. Immunol. *8*, 559–568. https://doi.org/10.1038/nri2314.
49. Senaldi, G., Shaklee, C.L., Guo, J., Martin, L., Boone, T., Mak, T.W., and Ulich, T.R. (1999). Protection against the mortality associated with disease models mediated by TNF and IFN-gamma in mice lacking IFN regulatory factor-1. J. Immunol. *163*, 6820–6826. https://doi.org/10.4049/jimmunol.163.12.6820.
50. Karaghiosoff, M., Steinborn, R., Kovarik, P., Kriegshäuser, G., Baccarini, M., Donabauer, B., Reichart, U., Kolbe, T., Bogdan, C., Leanderson, T., et al. (2003). Central role for type I interferons and Tyk2 in lipopolysaccharide-induced endotoxin shock. Nat. Immunol. *4*, 471–477. https://doi.org/10.1038/ni910.
51. Brown, S.D.M., Holmes, C.C., Mallon, A.M., Meehan, T.F., Smedley, D., and Wells, S. (2018). High-throughput mouse phenomics for characterizing mammalian gene function. Nat. Rev. Genet. *19*, 357–370. https://doi.org/10.1038/s41576-018-0005-2.
52. Buschmann, T. (2017). DNABarcodes: an R package for the systematic construction of DNA sample tags. Bioinformatics *33*, 920–922. https://doi.org/10.1093/bioinformatics/btw759.
53. Pandey, S., Takahama, M., Gruenbaum, A., Zewde, M., Cheronis, K., and Chevrier, N. (2020). A whole-tissue RNA-seq toolkit for organism-wide studies of gene expression with PME-seq. Nat. Protoc. *15*, 1459–1483. https://doi.org/10.1038/s41596-019-0291-y.
54. Soumillon, M., Cacchiarelli, D., Semrau, S., van Oudenaarden, A., and Mikkelsen, T.S. (2014). Characterization of directed differentiation by high-throughput single-cell RNA-Seq. bioRxiv. https://doi.org/10.1101/003236.
55. Srivastava, A., Sarkar, H., Gupta, N., and Patro, R. (2016). RapMap: a rapid, sensitive and accurate tool for mapping RNA-seq reads to transcriptomes. Bioinformatics *32*, i192–i200. https://doi.org/10.1093/bioinformatics/btw277.
56. Okonechnikov, K., Conesa, A., and García-Alcalde, F. (2016). Qualimap 2: advanced multi-sample quality control for high-throughput sequencing data. Bioinformatics *32*, 292–294. https://doi.org/10.1093/bioinformatics/btv566.
57. Ewels, P., Magnusson, M., Lundin, S., and Käller, M. (2016). MultiQC: summarize analysis results for multiple tools and samples in a single report. Bioinformatics *32*, 3047–3048. https://doi.org/10.1093/bioinformatics/btw354.
58. Smith, T., Heger, A., and Sudbery, I. (2017). UMI-tools: modeling sequencing errors in Unique Molecular Identifiers to improve quantification accuracy. Genome Res. *27*, 491–499. https://doi.org/10.1101/gr.209601.116.
59. Robinson, M.D., McCarthy, D.J., and Smyth, G.K. (2010). edgeR: a Bioconductor package for differential expression analysis of digital gene expression data. Bioinformatics *26*, 139–140. https://doi.org/10.1093/bioinformatics/btp616.
60. Ritchie, M.E., Phipson, B., Wu, D., Hu, Y., Law, C.W., Shi, W., and Smyth, G.K. (2015). limma powers differential expression analyses for RNA-sequencing and microarray studies. Nucleic Acids Res. *43*, e47. https://doi.org/10.1093/nar/gkv007.
61. Kuleshov, M.V., Jones, M.R., Rouillard, A.D., Fernandez, N.F., Duan, Q., Wang, Z., Koplev, S., Jenkins, S.L., Jagodnik, K.M., Lachmann, A., et al. (2016). Enrichr: a comprehensive gene set enrichment analysis web server 2016 update. Nucleic Acids Res. *44*, W90–W97. https://doi.org/10.1093/nar/gkw377.
62. Gu, Z., Eils, R., and Schlesner, M. (2016). Complex heatmaps reveal patterns and correlations in multidimensional genomic data. Bioinformatics *32*, 2847–2849. https://doi.org/10.1093/bioinformatics/btw313.
63. Gu, Z., Gu, L., Eils, R., Schlesner, M., and Brors, B. (2014). circlize Implements and enhances circular visualization in R. Bioinformatics *30*, 2811–2812. https://doi.org/10.1093/bioinformatics/btu393.
64. Dobin, A., Davis, C.A., Schlesinger, F., Drenkow, J., Zaleski, C., Jha, S., Batut, P., Chaisson, M., and Gingeras, T.R. (2013). STAR: ultrafast universal RNA-seq aligner. Bioinformatics *29*, 15–21. https://doi.org/10.1093/bioinformatics/bts635.
65. Liu, Y., Yang, M., Deng, Y., Su, G., Enninful, A., Guo, C.C., Tebaldi, T., Zhang, D., Kim, D., Bai, Z., et al. (2020). High-Spatial-Resolution Multi-omics Sequencing via Deterministic Barcoding in Tissue. Cell *183*, 1665–1681.e18. https://doi.org/10.1016/j.cell.2020.10.026.
66. Wolf, F.A., Angerer, P., and Theis, F.J. (2018). SCANPY: large-scale single-cell gene expression data analysis. Genome Biol. *19*, 15. https://doi.org/10.1186/s13059-017-1382-0.
67. van der Walt, S., Schönberger, J.L., Nunez-Iglesias, J., Boulogne, F., Warner, J.D., Yager, N., Gouillart, E., and Yu, T.; scikit-image contributors (2014). scikit-image: image processing in Python. PeerJ *2*, e453. https://doi.org/10.7717/peerj.453.
68. Traag, V.A., Waltman, L., and van Eck, N.J. (2019). From Louvain to Leiden: guaranteeing well-connected communities. Sci. Rep. *9*, 5233. https://doi.org/10.1038/s41598-019-41695-z.
69. Zepp, J.A., Morley, M.P., Loebel, C., Kremp, M.M., Chaudhry, F.N., Basil, M.C., Leach, J.P., Liberti, D.C., Niethamer, T.K., Ying, Y., et al. (2021).

Genomic, epigenomic, and biophysical cues controlling the emergence of the lung alveolus. Science *371*, eabc3172. https://doi.org/10.1126/science.abc3172.

70. Guilliams, M., Bonnardel, J., Haest, B., Vanderborght, B., Wagner, C., Remmerie, A., Bujko, A., Martens, L., Thoné, T., Browaeys, R., et al. (2022). Spatial proteogenomics reveals distinct and evolutionarily conserved hepatic macrophage niches. Cell *185*, 379–396.e38. https://doi.org/10.1016/j.cell.2021.12.018.
71. Novella-Rausell, C., Grudniewska, M., Peters, D.J.M., and Mahfouz, A. (2023). A comprehensive mouse kidney atlas enables rare cell population characterization and robust marker discovery. iScience *26*, 106877. https://doi.org/10.1016/j.isci.2023.106877.
72. Tabula; Muris Consortium (2020). A single-cell transcriptomic atlas characterizes ageing tissues in the mouse. Nature *583*, 590–595. https://doi.org/10.1038/s41586-020-2496-1.
73. Jin, S., Guerrero-Juarez, C.F., Zhang, L., Chang, I., Ramos, R., Kuan, C.-H., Myung, P., Plikus, M.V., and Nie, Q. (2021). Inference and analysis of cell-cell communication using CellChat. Nat. Commun. *12*, 1088. https://doi.org/10.1038/s41467-021-21246-9.
74. Hao, Y., Stuart, T., Kowalski, M.H., Choudhary, S., Hoffman, P., Hartman, A., Srivastava, A., Molla, G., Madad, S., Fernandez-Granda, C., et al. (2024). Dictionary learning for integrative, multimodal and scalable single-cell analysis. Nat. Biotechnol. *42*, 293–304. https://doi.org/10.1038/s41587-023-01767-y.
75. Kumar, N., Mishra, B., Athar, M., and Mukhtar, S. (2021). Inference of Gene Regulatory Network from Single-Cell Transcriptomic Data Using pySCENIC. Methods Mol. Biol. *2328*, 171–182. https://doi.org/10.1007/978-1-0716-1534-8_10.
76. Yu, G., Wang, L.G., Han, Y., and He, Q.Y. (2012). clusterProfiler: an R package for comparing biological themes among gene clusters. Omics *16*, 284–287. https://doi.org/10.1089/omi.2011.0118.
77. Gene Ontology Consortium (2021). The Gene Ontology resource: enriching a GOld mine. Nucleic Acids Res. *49*, D325–D334. https://doi.org/10.1093/nar/gkaa1113.
78. Martens, M., Ammar, A., Riutta, A., Waagmeester, A., Slenter, D.N., Hanspers, K., A Miller, R., Digles, D., Lopes, E.N., Ehrhart, F., et al. (2021). WikiPathways: connecting communities. Nucleic Acids Res. *49*, D613–D621. https://doi.org/10.1093/nar/gkaa1024.
79. Vahadane, A., Peng, T., Sethi, A., Albarqouni, S., Wang, L., Baust, M., Steiger, K., Schlitter, A.M., Esposito, I., and Navab, N. (2016). Structure-Preserving Color Normalization and Sparse Stain Separation for Histological Images. IEEE Trans. Med. Imaging *35*, 1962–1971. https://doi.org/10.1109/tmi.2016.2529665.
80. Schindelin, J., Arganda-Carreras, I., Frise, E., Kaynig, V., Longair, M., Pietzsch, T., Preibisch, S., Rueden, C., Saalfeld, S., Schmid, B., et al. (2012). Fiji: an open-source platform for biological-image analysis. Nat. Methods *9*, 676–682. https://doi.org/10.1038/nmeth.2019.

Please cite this article in press as: Clevenger et al., Whole-body molecular and cellular mapping of the laboratory mouse, Cell (2026), https://doi.org/10.1016/j.cell.2026.03.006

CellPress

STAR★METHODS

KEY RESOURCES TABLE

REAGENT or RESOURCE	SOURCE	IDENTIFIER
Antibodies		
Rat monoclonal anti-Ly6G (clone 1A8)	BioLegend	Cat# 127602; RRID:AB_1089180
Rat monoclonal anti-F4/80 (clone Cl:A3-1)	Bio-Rad	Cat# MCA497; RRID:AB_2098196
Rabbit monoclonal anti-Vimentin (clone D21H3)	Cell Signaling	Cat# 5741; RRID:AB_10695459
Chemicals, peptides, and recombinant proteins		
Lipopolysaccharide (LPS) from *Escherichia coli* O55:B5	Sigma-Aldrich	Cat# L2880-25MG
Phusion High-Fidelity DNA Polymerase	New England Biolabs	Cat# M0530L
T4 DNA ligase	New England Biolabs	Cat# M0202L
T4 DNA ligase buffer	New England Biolabs	Cat# B0202
Super-cryo embedding medium (SCEM)	SECTION-LAB Co. Ltd.	Cat# W-EM201
Mayer's Hematoxylin Solution	Sigma-Aldrich	Cat# MHS16-500ML
Eosin Y Solution, Aqueous	Sigma-Aldrich	Cat# HT110216-500ML
Pepsin from porcine gastric mucosa	Sigma-Aldrich	Cat# P7000-25G
Maxima H Minus Reverse Transcriptase	ThermoFisher Scientific	Cat# EP0753
RiboLock RNase inhibitor	ThermoFisher Scientific	Cat# EO0384
QIAGEN Proteinase K	Qiagen	Cat# 19131
Buffer PKD	Qiagen	Cat# 1034963
PureZOL™ RNA Isolation Reagent	Bio-Rad	Cat# 7326890
TURBO DNase™ (DNase I)	ThermoFisher Scientific	Cat# AM2239
Exonuclease I (*E. coli*)	New England Biolabs	Cat# M0293
Tagment DNA TDE1 Enzyme	Illumina	Cat# 20034197
Buffer RLT	Qiagen	Cat# 79216
Critical commercial assays		
ApopTag Plus Peroxidase In Situ Apoptosis Kit	Sigma-Aldrich	Cat# S7101
DNA Clean & Concentrator-5	Zymo Research	Cat# D4013
Advantage 2 PCR Kit	Takara Bio	Cat# 639206
NEBNext Ultra II Q5 Master Mix	New England Biolabs	Cat# M0544L
Qubit dsDNA Quantification Assay Kit, High Sensitivity	ThermoFisher Scientific	Cat# 32851
High Sensitivity D5000 ScreenTape	Agilent	Cat# 5067-5592
High Sensitivity D5000 Reagents	Agilent	Cat# 5067-5593
MinElute Gel Extraction Kit	Qiagen	Cat# 28604
SPRIselect DNA Size Selection Reagent	Beckman Coulter	Cat# B23318
Dynabeads MyOne Silane	ThermoFisher Scientific	Cat# 37002D
2% E-Gel EX Agarose Gels	ThermoFisher Scientific	Cat# G402002
Custom SureSelect DNA Capture Array (1M) microarray slide	Agilent Technologies	Cat# G3358A
1 Well ProPlate Slide Module	Electron Microscopy Sciences	Cat# 63484-31
Seal Strips	Electron Microscopy Sciences	Cat# 63484-80
Experimental models: Organisms/strains		
Mouse: C57BL/6J	The Jackson Laboratory	RRID:IMSR_JAX:000664
Mouse: B6.129S2-*Irf1*^{tm1Mak}/J	The Jackson Laboratory	RRID:IMSR_JAX:002762
Mouse: B6.129S(Cg)-*Stat1*^{tmDlv}/J	The Jackson Laboratory	RRID:IMSR_JAX:012606

(*Continued on next page*)

Please cite this article in press as: Clevenger et al., Whole-body molecular and cellular mapping of the laboratory mouse, Cell (2026), https://doi.org/10.1016/j.cell.2026.03.006

Continued

REAGENT or RESOURCE	SOURCE	IDENTIFIER
Oligonucleotides		
Array-seq anchor 1: CCCTACACGACGC TCTTCCGATCT	Cipurko et al.[10]	N/A
Array-seq anchor 2-UMI-$(dT)_{30}$VN: /5Phos/ GTAAAACGACGGCCAGNNNNNNNNNNNN NTTTTTTTTTTTTTTTTTTTTTTTTTTTTT*T*T*V*N	Cipurko et al.[10]	N/A
Array-seq template switching oligonucleotide (Array-seq): /5MeisodC//iisodG//iMe-isodC/ CCCTACACGACGCTCTTCCrGrGrG	Cipurko et al.[10]	N/A
Array-seq single-primer PCR primer: /5Biosg/CCCTACACGACGCTCTTCC	Cipurko et al.[10]	N/A
Array-seq and bulk RNA-seq library amplification forward primer: AATGATACGGCGACCACCGA GATCTACACTCTTTCCCTACA CGACGCTCTTCCG*A*T*C*T	Cipurko et al.[10]	N/A
Illumina i7 index primer (Array-seq and bulk RNA-seq) CAAGCAGAAGACGGCATAC GAGAT[i7]GTCTCGTGGGCTCGG	Illumina	Cat# FC-121-1011
Bulk RNA-seq custom RT primer:./5Biosg/ ACACTCTTTCCCTACACGACGCTCTTCC GATCT[6-bp-barcode]NNNNNNNNNN TTTTTTTTTTTTTTTTTTTTTTTTTTTTTVN	Soumillon et al.[54]	N/A
Bulk RNA-seq template switching oligonucleotide: iCiGiCACACTCT TTCCCTACACGACGCrGrGrG	Soumillon et al.[54]	N/A
Bulk RNA-seq single-primer PCR primer: /5Biosg/ACACTCTTTCCCTACACGACGC	Soumillon et al.[54]	N/A
Software and algorithms		
DNABarcodes	Buschmann[52]	https://www.bioconductor.org/packages/release/bioc/html/DNABarcodes.html
BaseSpace DRAGEN Analysis v1.3.0	Illumina	https://www.illumina.com/products/by-type/informatics-products/dragen-secondary-analysis.html
STARsolo (STAR v2.7.10a)	Dobin et al.[64]	https://github.com/alexdobin/STAR/blob/master/docs/STARsolo.md
Scanpy	Wolf et al.[66]	https://github.com/scverse/scanpy
Wand	McConville (GitHub)	https://github.com/emcconville/wand
scikit-image	van der Walt[67]	https://scikit-image.org/
CellKb	Patil et al.[19]	https://www.cellkb.com/
CARD	Ma et al.[22]	https://github.com/YMa-lab/CARD
RCTD	Cable et al.[20]	https://github.com/dmcable/spacexr
Cell2location v0.1.5	Kleshchevnikov et al.[21]	https://github.com/BayraktarLab/cell2location
Vahadane stain normalization algorithm	Vahadane et al.[79]	https://github.com/CielAI/torch-staintools
UNI foundation model	Chen et al.[11]	https://github.com/mahmoodlab/UNI
CellChat	Jin et al.[73]	https://github.com/sqjin/CellChat
Seurat	Hao et al.[74]	https://satijalab.org/seurat/
pySCENIC v0.12.1	Kumar et al.[75]	https://github.com/aertslab/pySCENIC
clusterProfiler	Yu et al.[76]	https://github.com/YuLab-SMU/clusterProfiler
RapMap	Srivastava et al.[55]	https://github.com/COMBINE-lab/RapMap
FastQC	Babraham Bioinformatics	https://www.bioinformatics.babraham.ac.uk/projects/fastqc/

(*Continued on next page*)

Please cite this article in press as: Clevenger et al., Whole-body molecular and cellular mapping of the laboratory mouse, Cell (2026), https://doi.org/10.1016/j.cell.2026.03.006

Continued

REAGENT or RESOURCE	SOURCE	IDENTIFIER
Qualimap	Okonechnikov et al.[56]	http://qualimap.conesalab.org/
MultiQC	Ewels et al.[57]	https://github.com/ewels/MultiQC
UMI-tools	Smith et al.[58]	https://github.com/vals/umis
edgeR	Robinson et al.[59]	https://github.com/StoreyLab/edge
limma	Ritchie et al.[60]	https://bioconductor.org/packages/release/bioc/html/limma.html
Enrichr	Kuleshov et al.[61]	http://amp.pharm.mssm.edu/enrichr/
ComplexHeatmap	Gu et al.[62]	https://github.com/jokergoo/ComplexHeatmap
circlize	Gu et al.[63]	https://github.com/jokergoo/circlize
FIJI	Schindelin et al.[80]	https://imagej.net/software/fiji/
Deposited data		
Analysis code repository	This paper	GitHub: https://github.com/chevrierlab/WMST-paper
Analysis scripts	This paper	Zenodo: https://doi.org/10.5281/zenodo.15741906
LABEL computational pipeline for virtual staining	This paper	Code Ocean: https://doi.org/10.24433/CO.3645054.v1

EXPERIMENTAL MODEL AND STUDY PARTICIPANT DETAILS

Mice

Female C57BL/6J (stock 000664), *Irf1*$^{-/-}$ (B6.129S2-*Irf1*^{tm1Mak}/J; stock 002762), and *Stat1*$^{-/-}$ (B6.129S(Cg)-*Stat1*^{tmDlv}/J; stock 012606) mice were obtained from the Jackson Laboratories. Animals were housed in specific pathogen-free conditions at The University of Chicago and all experiments were performed in accordance with the US National Institutes of Health Guide for the Care and Use of Laboratory Animals and approved by The University of Chicago Institutional Animal Care and Use Committee.

METHOD DETAILS

Mouse lipopolysaccharide injections

To induce endotoxemia with lipopolysaccharide (LPS), 6-week-old mice were injected intraperitoneally with a sublethal dose of LPS (3–5 mg/kg) derived from Escherichia coli O55:B5 (Sigma-Aldrich, L2880-25MG) diluted in PBS. Dosing was established for each lot of LPS by *in vivo* titration. Control animals were injected intraperitoneally with PBS only or left untreated.

Custom oligonucleotide microarray design for Array-seq slides

We used a custom array design for the microarray platform SureSelect DNA Capture Array (1 M; Agilent, G3358A) to obtain Array-seq slides for spatial transcriptomics profiling as described.[10] For spatial barcodes (18-mer), we used the DNABarcodes R package[52] to design them as follows. We first created 9-mer barcodes with a minimum Hamming distance of 3, no self-complimentary sequences, no consecutive base repetition $\geq$ 3, and with a 50% GC content. Resulting barcodes were duplicated and concatenated in all possible 2-way combinations, creating a pool of over 6.5 million, 18-mer barcodes which maintained the minimum Hamming distance of 3 as in the original set. Barcode sequences were filtered to maximize sequencing performance using the following criteria: (1) does not begin with AC or CC, (2) does not end with GG, and (3) no consecutive base repetition $\geq$ 3. After filtering, we obtained 5,069,490 unique barcode sequences from which a random set of 974,016 barcodes was selected.

Array-seq slide preparation

Custom SureSelect DNA Capture Array (1M) (Agilent, G3358A) microarrays were attached to a gasket with a 1 Well ProPlate Slide Module (Electron Microscopy Sciences, 63484–31). To assemble mRNA-capture probes, two oligos: Anchor 1 (5′-CCCTACAC GACGCTCTTCCGATCT-3′) and Anchor 2-UMI-(dT)$_{30}$VN (5′-
/5Phos/GTAAAACGACGGCCAGNNNNNNNNNNNNTTTTTTTTTTTTTTTTTTTTTTTTTTTTTT*T*T*V*N-3′) (500 nM each) were hybridized to probes on the array in duplexing buffer (IDT, 11-01-03-01). After adding soluble oligos into the 1-well module, we sealed the module (Electron Microscopy Sciences, 63484-80) and incubated the array for 1 hour at 45°C on an *in situ* hybridization (ISH) adapter (Techne, EAR99) in a thermocycler (Mastercycler X50a, Eppendorf, 6313000018). After hybridization, arrays were washed using a three-step procedure with the following buffers consecutively for 1 min in the chamber on the array: 0.1% Tween-20 (Sigma, P7949-500ML) in 1X PBS, 0.01% Triton X-100 (Sigma, T8787-50ML) in 1X PBS, and 1X PBS. Next, we prepared an extension-ligation reaction mix consisting of 1X T4 Ligase Buffer (NEB, M0202L), 0.2 mg/mL BSA (Sigma, B86671.25ML), 50 mM KCl (Millipore Sigma, P3911), 100 μM dNTPs (NEB, N0447), 5 mM ATP (NEB, P0756L), 0.05 U/μL Phusion High-Fidelity DNA Polymerase (NEB, M0530L), and 30 U/μL T4 DNA ligase (NEB, B0202). The extension-ligation reaction mix was added to the chamber on the array, the chamber

Please cite this article in press as: Clevenger et al., Whole-body molecular and cellular mapping of the laboratory mouse, Cell (2026), https://doi.org/10.1016/j.cell.2026.03.006

was sealed, and the array was incubated overnight at 37°C. After extension-ligation, arrays were washed using the three-step procedure detailed above. Lastly, to remove unligated Anchor 2-UMI-Oligo(dT) oligonucleotides, the array was incubated for 10 minutes at 58°C in 25 mM NaCl and 25 mM Tris-HCl (pH = 7.4) (Bioworld, 21420063-1). The array was washed using the three-step procedure detailed above, washed briefly with nuclease-free water, detached from the chamber, air-dried, and stored at 4°C in a sealed, opaque 50-mL conical tube (Thermo Fisher Scientific, 50550-489) until use.

Whole-mouse histological sectioning

6-week-old mice were euthanized with CO_2 then massaged with a depilatory agent (NAIR) until all hair was removed. Mice were then placed in a plastic bag, frozen in a dry ice-hexane bath, and stored -80°C or immediately processed for embedding as follows. Fresh-frozen mice were placed in a freezing frame containing embedding medium SCEM (SECTION-LAB Co. Ltd., W-EM201) and placed into a dry ice-hexane bath until all the media was frozen. Frozen specimens were sectioned (10-μm thickness) using a cryomacrotome (Leica CM3600XP). Once an appropriate cross-sectional block face profile was obtained (all major organs described in the paper are visible on the gross tissue block), a transfer cryotape film (SECTION-LAB Co. Ltd.) was applied to the frozen block surface as described in the Kawamoto film method.[13] Whole-mouse sections collected on the transfer film were gently mounted onto Array-seq slides, briefly thawed at room temperature prior to re-freezing and transfer film removal using 95% n-hexane (Fisher Scientific, AC197360050).

Whole-mouse H&E staining and imaging

Whole-mouse sections transferred on Array-seq slides were fixed for 30 minutes at -20°C in 100% methanol (Sigma-Aldrich, 32213). Fixed sections were incubated for 1 minute at room temperature in isopropanol (Sigma-Aldrich, I9516) and air dried for 3 minutes at room temperature. Hematoxylin (Sigma-Aldrich, MHS16-500ML) and eosin (Sigma-Aldrich, HT110216-500ML) were filtered through a 0.22-μm sterile filter (Foxx Life Sciences, 371-2215-OEM) before use. Upon drying, sections were stained for 3 minutes at room temperature with hematoxylin, washed in nuclease-free water, and stained for 1 minute at room temperature with eosin diluted 1:10 in 0.45 M Tris-Acetic acid buffer, pH = 6.0 (Sigma-Aldrich, GE17-1321-01 and A6283). The slide was washed in nuclease-free water, kept at room temperature until dry, and imaged at 20X magnification using an Olympus VS2000 slide scanner.

Whole-mouse section permeabilization and reverse transcription for Array-seq

Array-seq slides with H&E-stained whole-mouse sections were attached to a 1 Well ProPlate Slide Module (Electron Microscopy Sciences, 63484-31). Sections were permeabilized with 0.1% pepsin (Sigma, P7000-25G) in 0.1 M HCl (ColeParmer, EW-88011-96) for 20 min at 37°C. After permeabilization, sections were washed once with 0.1X saline-sodium citrate (SSC) buffer (Sigma, S6639-1L). After removing the wash buffer, a 1.5-mL reverse transcription mix consisting of 1X Maxima Reverse Transcriptase Buffer (ThermoFisher Scientific, EP0753), 0.2 mg/mL BSA (Sigma, B8667-1.25ML), 0.5 mM dNTPs (NEB, N0447L), 3 μM of template switching oligonucleotide (TSO) (5'-/5MeisodC//iisodG//iMe-isodC/CCCTACACGACGCTCTTCCrGrGrG-3'), 2 U/μL Ribolock (ThermoFisher Scientific, EO0384), and 10 U/μL Maxima H Minus Reverse Transcriptase (Thermo Fisher Scientific, EP0753) was added to the 1-well module, sealed, and incubated overnight at 42°C. The array was washed once with 0.1X SSC and incubated for 1 hour at 37°C using a tissue removal buffer containing Proteinase K (Qiagen, 19131) at 1:8 dilution in buffer PKD (Qiagen, 1034963). The array was washed once with 0.1X SSC followed by buffer EB (Qiagen, 19086), and full-length cDNAs were eluted from the array by incubating for 10 minutes at room temperature in 0.1 M KOH (Sigma, P4494-50ML). Equal volumes of eluted cDNAs were transferred into 4 separate 1.5-mL tube and neutralized by adding 0.2X volume of 1M Tris-HCl (pH=7.4; APEX, 18-189).

Array-seq library preparation and sequencing

Each aliquot of cDNAs were purified using a DNA Clean & Concentrator-5 kit (Zymo Research, D4013) and amplified using single-primer PCR with the following primer: 5'-/5Biosg/CCCTACACGACGCTCTTCC-3' using the Advantage 2 PCR Kit (Takara, 639206) in a 50-μL reaction volume and with the following cycling conditions: 1 cycle at 95°C for 1 min; 8 cycles at 95°C for 15 sec, 65°C for 30 sec, 68°C for 6 min; and 1 cycle at 72°C for 10 min. Amplified cDNAs were cleaned up using 0.6X volume of magnetic SPRISelect beads (Beckman Coulter, B23318) and quantified using the Qubit dsDNA High Sensitivity Assay Kit (ThermoFisher Scientific, 32851) and a TapeStation D5000 high sensitivity DNA Screentape kit (Agilent). Amplified cDNAs were pooled and 100 ng of cDNA was tagmented using Tagment DNA TDE1 Enzyme and buffer (Illumina, 20034197) for 5 min at 55°C. Tagmented cDNAs were cleaned up using DNA Clean & Concentrator-5 columns (Zymo Research, D4013) and amplified by PCR using the NEBNext Ultra II Q5 Master Mix (NEB, M0544S) and the following forward primer: 5'-

AATGATACGGCGACCACCGAGATCTACACTCTTTCCCTACACGACGCTCTTCCG*A*T*C*T-3' and Illumina i7 reverse primer (Illumina, FC-121-1011) with the following cycling conditions: 1 cycle at 98°C for 30 sec; 8 cycles at 98°C for 10 sec, 63°C for 30 sec and 65°C for 30 sec; and 1 cycle at 65°C for 5 min. Libraries were cleaned up using 0.8X volume of magnetic

SPRISelect beads followed by gel purification using 2% E-Gel EX agarose Gels (Thermo Fisher Scientific G402002) and MinElute columns (Qiagen, 28604) and quantified with the Qubit dsDNA High Sensitivity Assay Kit (Thermo Fisher Scientific 32851). Resulting libraries were sequenced on the Novaseq 6000 platform (Illumina) with 44 bases for read 1, 8 bases for i7 barcodes, and 70 bases for read 2.

Please cite this article in press as: Clevenger et al., Whole-body molecular and cellular mapping of the laboratory mouse, Cell (2026), https://doi.org/10.1016/j.cell.2026.03.006

CellPress

Mouse tissue harvest for for whole-tissue RNA-seq

Mouse tissues from 6-week-old mice were harvested as previously described.[53] Mice were anesthetized with 2,2,2-tribromoethanol (250–500 mg/kg) and perfused transcardially with PBS containing 10 mM EDTA to remove blood from all organs. Immediately after perfusion, tissues were placed in homemade RNA-preserving solution (5.3 M ammonium sulfate, 25 mM sodium citrate, 20 mM EDTA) and kept at 4°C overnight then transferred to -80°C for storage prior to tissue lysis followed by RNA extraction.

Whole-tissue RNA extraction

Whole-tissue RNA extraction was performed as described previously.[53] Briefly, mouse tissues stored in RNA-preserving solution were thawed and transferred to 2 mL tubes containing 700–1500 μL (depending on tissue) of PureZOL (Bio-Rad, 7326890) or homemade Trizol-like solution (38% phenol, 0.8 M guanidine thiocyanate, 0.4 M ammonium thiocyanate, 0.1 M sodium acetate, 5% glycerol). Tissues were lysed by adding 2.8-mm ceramic beads (OMNI International, 19–646) and running 1-3 cycles of 5-45 s at 3500 rpm on the PowerLyzer 24 (Qiagen). For liver, brain, and small intestine samples, tissues were lysed with 3-5 mL using M tubes (Miltenyi biotec, 130-096-335) and running 1-4 cycles of the RNA_02.01 program on the gentleMACS Octo Dissociator (Miltenyi biotec). Next, lysates were processed in deep 96-well plates (USA Scientific 1896-2000) by adding chloroform for phase separation by centrifugation, followed by precipitation of total RNA in the aqueous phase using magnetic beads coated with silane (Dynabeads MyOne Silane; TermoFisher Scientific 37002D), buffer RLT (Qiagen 79216), and ethanol. Genomic DNA contamination was removed by on-bead DNase I (ThermoFisher Scientific AM2239) treatment at 37 °C for 20 min. After washing steps with 80% ethanol, RNA was eluted from beads. RNA extraction was performed on the Bravo Automated Liquid Handling Platform (Agilent). Sample concentrations were measured using a Nanodrop 8000 (Thermo Scientific). RNA quality was evaluated using a Tapestation 4200 (Agilent Technologies).

Whole-tissue RNA sequencing

For each tissue sample, full-length cDNA was synthesized in 20 μl final reaction volume containing the following: (1) 10 μl of 10 ng/μl RNA; (2) 1 μl containing 2 pmoles of a custom RT primer[54] (5'-/5Biosg/ACACTCTTTCCCTACACGACGCTCTTCCGATCT[6-bp barcode]NNNNNNNNNN-3') that is biotinylated in 5' and contains sequences from 5' to 3' for the Illumina Read 1 primer, a 6-bp sample barcode (up to 384), a 10-bp unique molecular identifier (UMI), and an anchored oligo(dT)$_{30}$ for priming; and (3) 9 μl of RT mix containing 4 μl of 5X RT buffer, 1 μl of 10 mM dNTPs, 2 pmoles of template switching oligo (5'-iCiGiCACACTCTTTCCCT ACACGACGCrGrGrG-3'),[54] and 0.25 μl of Maxima H Minus Reverse Trascriptase (Thermo Scientific, EP0753). First, barcoded RT primers were added to RNA, which were then denatured at 72°C for 1 min and snap cooled on ice. Second, the RT mix was added, and plates were incubated at 42°C for 120 min. For each library, double stranded cDNA from up to 384 samples at a time were pooled using DNA Clean & Concentrator-5 columns (Zymo Research, D4013), and residual RT primers were removed using exonuclease I (New England Biolabs, M0293). Full-length cDNAs were amplified with 5 to 8 cycles of single-primer PCR using the Advantage 2 PCR Kit (clontech 639206) and the following primer: 5'-/5Biosg/ACACTCTTTCCCTACACGACGC-3'. cDNA was cleaned up using SPRIselect magnetic beads (Beckman Coulter B23318) and quantified with a Qubit dsDNA High Sensitivity Assay Kit (ThermoFisher Scientific 32851). 50 ng of cDNA per pool of samples was tagmented using the Tagment DNA Enzyme I (Illumina 20034197) and amplified using the NEBNext Ultra II Q5 Master Mix (NEB, M0544L) with with the following forward primer: 5'-

AATGATACGGCGACCACCGAGATCTACACTCTTTCCCTACACGACGCTCTTCCG*A*T*C*T-3' and Illumina i7 reverse primer (Illumina, FC-121-1011). Libraries were gel purified using 2% E-Gel EX Agarose Gels (ThermoFisher Scientific G402002), quantified with a Qubit dsDNA High Sensitivity Assay Kit (ThermoFisher Scientific Q32851) and a Tapestation 4200 (Agilent Technologies), and sequenced on the NextSeq 550 platform (Illumina).

Immunohistochemistry

Paraformaldehyde-fixed, paraffin-embedded mouse tissues (lung, spleen, thymus, liver, kidney, colon) from 6-week-old mice were sectioned at 5 μm thickness and processed for immunostaining and TUNEL assays using standard procedures. In brief, heat-induced antigen retrieval was performed in citrate buffer (pH 6). Slides were quenched with 0.3% H_2O_2, subjected to streptavidin/biotin blocking, and then serum blocked with normal serum matched to the secondary antibody host. Primary antibodies included anti-Ly6G (clone 1A8, BioLegend 127602), anti-F4/80 (clone CI:A3-1, Bio-Rad MCA497), and anti-Vimentin (clone D21H3, Cell Signaling 5741), TUNEL staining was performed using the In Situ Cell Death Detection Kit (Sigma S7101), and all sections were counterstained with hematoxylin. Whole-slide images were captured on a Hamamatsu NanoZoomer S360MD slide scanner system at 40X magnification.

QUANTIFICATION AND STATISTICAL ANALYSIS

Bulk mouse tissue RNA sequencing data analysis

Raw read processing and quantification

Sequencing read files were processed to generate UMI (unique molecular identifier) count matrices using the python toolkit from the bcbio-nextgen project version 1.1.5 (https://bcbio-nextgen.readthedocs.io/en/latest/). In brief, reads were aligned to the mouse mm10 transcriptome with RapMap[55] (https://github.com/COMBINE-lab/RapMap). Quality control metrics were compiled with a

Please cite this article in press as: Clevenger et al., Whole-body molecular and cellular mapping of the laboratory mouse, Cell (2026), https://doi.org/10.1016/j.cell.2026.03.006

combination of FastQC (http://bioinformatics.babraham.ac.uk/projects/fastqc/), Qualimap,[56] MultiQC[57] (https://github.com/ewels/MultiQC). Samples were demultiplexed using barcodes stored in Read 1 (first 6 bases) and raw UMI count matrices were computed using UMIs stored in Read 1 (bases 7 to 16) (https://github.com/vals/umis).[58]

Differential expression and pathway analysis

Differential expression (DE) analysis was done using custom scripts in R (http://www.R-project.org). Raw count matrices were filtered to keep genes with at least 20 counts per million (cpm) or 5 UMIs in 2 samples and normalized across samples using the calcNormFactor function in edgeR[59] (https://github.com/StoreyLab/edge). We identified genes with indicated Benjamini and Hochberg FDR adjusted p value by comparing treated tissues and matching control tissues using limma.[60] Transcription factor enrichment analysis was performed on inflammatory differentially expressed genes using Enrichr[61] (http://amp.pharm.mssm.edu/enrichr/) with the TRRUST_Transcription_Factors_2019 database. All heatmaps were generated using ComplexHeatmap (https://github.com/jokergoo/ComplexHeatmap) and circlize (https://github.com/jokergoo/circlize) packages in R.[62,63]

Whole-mouse spatial transcriptomics data analysis

Spatial gene expression matrix generation

Fastq files from Array-seq sequencing experiments were generated using BaseSpace DRAGEN Analysis v1.3.0 (Illumina). The spatial barcodes and UMIs are contained in the Read 1 sequence (spatial barcode: 1–18 bases, UMI: 35–44 bases) while the Read 2 sequence contains cDNA information. To generate spatial count matrices, fastq files were processed using STARsolo from the STAR package version 2.7.10a (https://github.com/alexdobin/STAR/blob/master/docs/STARsolo.md).[64] Reads were aligned to the mm10 mouse reference genome (GRCm38), spatial barcodes were demultiplexed against the whitelist of the reverse complement sequences of the 974,016 Array-seq spatial barcodes (using the Exact option), and unique molecular identifiers (UMIs) were collapsed (using the 1MM_CR option for error correction).

Alignment of spatial data with H&E image

To filter the Array-seq data to only include spots under tissue areas from whole-mouse sections, we followed similar procedures described by others[65] with modifications as described below. STARsolo output count matrices were read into Python 3.8.5 (http://www.python.org) with Scanpy[66] and stored in an AnnData object together with the spatial coordinates of each barcoded spot on the slide. The spot coordinates and UMI counts were used to generate a scalable vector graphic (svg) image composed of points matching the x, y positions of each barcoded spot which were colored based on UMI counts. The svg image was converted to a png format using the Wand package (https://github.com/emcconville/wand) and manually aligned with the H&E image of the same section using Illustrator (Adobe). The *x* and *y* positions, height, and width of the aligned images were recorded. The spatial transcriptomics AnnData object was imported, scaled to match the corresponding pixel coordinated of the H&E image, and filtered to remove spots not under the detected tissue using the scikit-image package.[67]

Clustering and differential expression

For spatial gene expression analysis using Scanpy, resulting count matrices were further filtered to keep (1) genes with at least 20 UMIs across all spots, and (2) spots with more than 300 UMIs in total. Data was normalized, log10 transformed, and clustered using principal component analysis (PCA) and the k-nearest neighbors (KNN) and Leiden[68] algorithms. For plotting, spatial count or clustering data were overlaid on the grayscale H&E image using Seaborn (https://seaborn.pydata.org/). Organ annotations were mapped to each cluster based upon spatial localization when overlayed on the aligned H&E image. Clusters that did not correspond to a clearly identifiable major organ were labeled as "Other", representing spatial transcriptomic spots not confidently assigned to a specific organ at this stage. To map anatomical subregions, raw unnormalized data from the spots identified from each organ were subsetted from the dataset, clustered as described above, and annotated based upon spatial localization in the H&E image in addition to the top 15 differentially expressed genes from each cluster. To resolve finer tissue structures, spots within each annotated organ were downsampled and jointly reclustered with spots assigned to "Other" in the organ annotation. Features were reduced using TruncatedSVD on highly variable genes derived from major organs and "Other" spots, followed by KNN graph construction, Leiden clustering,[68] and UMAP visualization. Clusters were annotated based on spatial localization in the H&E image and top differentially expressed genes were inspected for clusters corresponding to newly identified structures. For differential expression analyses, we used the tl.rank_genes_groups() function in Scanpy to calculate differentially expressed genes either across annotated spatial regions or across broad cell types within anatomical regions. The percentage of differentially expressed (DE) genes per core cell type in each organ was calculated as follows:

$$P_{C_i j} = \frac{\left|\bigcup\{DE_{b j} | b \in C_i\}\right|}{\sum_k \left|\bigcup\{DE_{b j} | b \in C_k\}\right|},$$

where C_i is the core cell type i, b is a broad cell type, j indicates the organ type, and $DE_{b,j}$ refers to the differentially expressed gene set from broad cell type b and organ j. The significance threshold for differentially expressed genes is set as $FDR < 0.05, |log_2\ FC| > 0.25$.

Spatial assignment of cell types

To systematically assess the spatial assignment of cell types across whole-mouse sections, we used the CellKb database (https://www.cellkb.com) to infer the cell type composition for each Array-seq spot under whole-mouse sections.[19] CellKb contains a

curated collection of cell type-specific gene signatures derived from publicly available single-cell RNA-seq studies, where each dataset was processed using the original publication's workflow for quality control, normalization, and clustering, with no additional batch correction applied beyond what was reported in the source study. Marker gene lists were obtained directly from supplementary materials or, when absent, recalculated from normalized expression values using the Wilcoxon rank-sum test. Harmonization was performed at the annotation level by assigning tissue and cell type using standardized Uberon Ontology and Cell Ontology terms, respectively. Final signatures were compiled as ranked gene lists, enabling robust rank-based matching across datasets with different preprocessing pipelines.

Using single-cell RNA-seq data from 284 publications covering 54M cells, we obtained 9,692 gene signatures covering 495 cell types across the 16 mouse tissue types identified in the dataset (Tables S1A and S1B). Spots assigned to one of these 16 organs were annotated using the corresponding organ-specific signatures. To annotate spots assigned to "Other" in the organ-level clustering, we used single-cell data from an additional 182 publications, spanning 54+ additional organs (*e.g.*, adrenal gland, uterus, esophagus) and smaller anatomical structures (*e.g.*, dorsal root ganglion, myenteric nerve plexus, cochlea). In total, this reference comprised 466 publications covering a total of 59M cells, resulting in 18,745 total gene signatures covering 793 cell types (Tables S1A and S1B). For each spot, 500 spot-specific genes with the highest positive log fold change compared to all other spots were calculated. This ranked gene list was compared to all gene signatures from a specific tissue in CellKb using a rank-based method. For each spot-specific gene list, the rank-based method assigned a match score to every gene signature in CellKb based on (a) the number of overlapping genes with the gene signature, (b) the ranks of the overlapping genes, (c) the rank differences of the overlapping genes, and (d) the number of genes in the gene signature. Based on the scores of the top 100 matching gene signatures, the proportion of each cell type per spot was calculated as follows:

$$Proportion\ of\ cell\ i, P_i = (M_i - \overline{M}) + (0.1 * [\overline{M} * (n_i - 1)]),$$

where M_i is the match score of the first matching marker gene set of cell type i; $\overline{M}$ is the average match score of the top 20 matching marker gene sets; and n_i is the number of matching marker gene sets of cell type i in the top 20.

Top 3 positive cell type proportions, P_i, are normalized such that their sum is 1 and assigned to the spot. We also classified the cell types into 79 broad and 30 core cell types to facilitate some of the downstream analyses and visualizations of the spatial data (Table S1C). Cell types were manually assigned to broad and core classes based on the parent cell types in the Cell Ontology annotations.

To benchmark CellKb spot-level cell type inference, we applied CARD[22], RCTD,[20] and Cell2location[21] (v0.1.5, implemented in scvi-tools v1.3.3) to all spots from each replicate in the Array-seq dataset for spleen, lung, liver, and kidney using organ-specific reference datasets.[69–72] Each organ was analyzed separately using raw UMI counts and organ-matched single-cell references. Sample identity was encoded in the single-cell references for all reference datasets, and spatial inference was performed per Array-seq sample. Single-cell references were filtered to retain cell types with at least 25 cells and genes detected in ≥5 cells and reference genes restricted to overlap with the corresponding Array-seq dataset. For RCTD, doublet detection was used to model mixed spots. For Cell2location, the regression reference model was trained for 250 epochs, and the spatial model was trained for 30,000 epochs with N_cells_per_location = 10 and detection_alpha = 20. CARD was performed with standard regularization settings. Predicted compositions were harmonized at the broad cell type level. Agreement of comparator methods with CellKb was quantified per-replicate, per-organ, as:

$$Agreement = \frac{1}{N_{spots}} \sum_{i=1}^{N_{spots}} 1\left(y_i^{CellKb} \in \left\{y_{i,1}^{CM}, y_{i,2}^{CM}, y_{i,3}^{CM}\right\}\right),$$

where y_i^{CellKb} is the top CellKb assignment for spot i, CM is the comparator method and $y_{i,1-3}^{CM}$ are the top 3 predictions from each comparator method.

Ligand-receptor analysis

Ligand-receptor signaling was inferred with CellChat[73] using a spatial workflow applied separately to each indicated sample. Seurat[74] objects were built from all four samples per organ, log-normalized, and split into Control or LPS groups before constructing CellChat objects with spatial coordinates, broad cell type labels and sample annotations. For each sample and signaling class (Secreted and Cell-Cell Contact), we identified overexpressed genes and ligand receptor interactions, smoothed expression values using the mouse protein-protein interaction graph and computed spatially constrained communication probabilities with the function computeCommunProb using a truncated mean estimator. Interaction windows were restricted to organ boundaries and defined as 8X pitch for secreted signaling and 3X pitch with a 2X pitch contact window for cell-cell contact interactions, with probabilities weighted by intercellular distance and normalized by population size. Interactions supported by fewer than five expressing cells were removed and pathway-level aggregation was performed to infer pathway-specific communication probabilities. Treatment-specific CellChat objects were merged to enable four-way sample comparison, and pathway-level and ligand receptor-level differences were quantified using rankNet and netAnalysis_contribution, with pathways that showed condition-specific signaling strengths and their top ligand receptor contributors carried forward for organ-specific interpretation.

Inference of STAT1 and IRF1 regulons

Regulatory network analysis was performed using pySCENIC[75] (v0.12.1) on per-organ, per-core cell type datasets (≥800 spots per core cell type), constructed from spots in which the core cell type was the dominant assignment, using only LPS-treated replicates.

Please cite this article in press as: Clevenger et al., Whole-body molecular and cellular mapping of the laboratory mouse, Cell (2026), https://doi.org/10.1016/j.cell.2026.03.006

Gene regulatory networks were inferred with GRNBoost2 using IRF1 and STAT1 as candidate transcription factors and the union of variable genes identified across all organ-core cell type datasets as input genes. Motif-based refinement was performed with the mm10 motif database to identify high-confidence regulons based on motif similarity ($Q \leq 0.001$), normalized enrichment score (NES ≥ 3.2), and occurrence in ≥ 2 motifs. Regulon activity was quantified with AUCell (auc_max_rank = 1000) per spot in LPS and control replicates for each organ and core cell type, and ΔAUC values were calculated as the difference between mean AUC in LPS and control samples. Regulon genes were clustered as described in the figure legends, and pathway enrichment analysis was performed on clustered regulon gene sets using clusterProfiler[76] with Gene Ontology Biological Process[77] and WikiPathways[78] databases accessed through Enrichr.[61]

STAT1- and IRF1-dependent gene signature scoring

To assess transcriptional responses to LPS attributable to IRF1 and STAT1 signaling, we derived gene signatures from the differentially expressed genes identified in the whole-tissue, bulk RNA-seq analysis described above. Differentially expressed genes were grouped by tissue of origin and experimental comparison: either LPS-treated *Irf1*$^{-/-}$ or *Stat1*$^{-/-}$ mice versus LPS-treated wild-type controls, or LPS-treated wild-type versus untreated wild-type mice. Genes were further divided by directionality (up- or downregulated) to identify genes whose LPS-induced changes were reversed in either knockout background, yielding tissue-specific positive and negative signatures for IRF1 and STAT1 dependent responses. To apply these signatures to the spatial transcriptomic dataset, the dataset was subsetted by organ, normalized, $\log_{10}$-transformed, and gene set enrichment scores were calculated per-spot using Scanpy's tl.score_genes, using only genes present in the corresponding organ-specific dataset.

LABEL algorithm for the virtual staining of histology H&E images

In our custom-built LABEL algorithm, histology features were extracted from H&E images obtained from whole-mouse sections, including Array-seq–associated samples and additional H&E-only sections, using a foundation model for computational pathology. To harmonize H&E staining between Array-seq–associated images and the H&E-only dataset, we applied the Vahadane stain-normalization algorithm[79] using a representative reference image selected from the H&E-only whole-mouse dataset, and normalized the four whole-mouse sections with matched H&E and Array-seq data to this reference. Each Array-seq-associated normalized tissue section was segmented into image patches centered on spatial transcriptomic capture spots. Each patch was resized to 224×224 pixels, and input to the UNI pathology foundation model[11] (https://github.com/mahmoodlab/UNI) to extract 1,536-dimensional representations. Multiple H&E patch sizes (32, 64, 128, 256, and 512 pixels) were evaluated, and a patch size of 128×128 pixels was selected for optimal performance. Second, our LABEL algorithm uses a spatially aware K-nearest neighbor (KNN) classifier ($k = 5$) to perform hierarchical classifications of organs, subregions, and cell types in mouse tissues. For each H&E image patch, the spatial coordinates of its center were concatenated with the UNI-extracted feature vector and reduced to 200 dimensions by principal component analysis (PCA). Classification of test-set patches and prediction of patches from additional tissue sections was performed by identifying the five nearest neighbors in this reduced PCA space from the training set and assigning annotations by majority vote. For evaluation purposes, training and test sets were either randomly split into a 3% training group and 20% evaluation group across the four whole-mouse sections with matching H&E and Array-seq data (i.e., "in-distribution" split) or formed by leaving one whole-mouse section out for testing while training on the remaining three whole-mouse sections (i.e., "leave-one-out" split). Independent KNN classifiers were fitted at each hierarchical level (organ, subregion, and broad cell type). For cross-validation, normalized confusion matrices were restricted to entities present in both whole-mouse section replicates from control mice, and broad cell types were limited to those with at least 0.1% abundance in these control mouse datasets. Each element (i,) in a normalized confusion matrix shows the proportion of true class i predicted as class j, referred to as the accuracy score. Predictions were also generated for H&E-only whole-mouse sections using the trained KNN classifiers to assess model generalization to independent H&E data.

Immunohistochemistry image data analysis

Quantification of positive staining was performed in FIJI[80] by color deconvolution, thresholding and particle analysis to determine the positively stained area (μm^2) or number of 3,3′-diaminobenzidine-positive (DAB+) cells per field of view (FOV), summarized across 4–8 FOVs per biological replicate. Statistical comparisons between LPS-treated and control groups were made using a one-sided Mann-Whitney U test.

CellPress

Supplemental figures

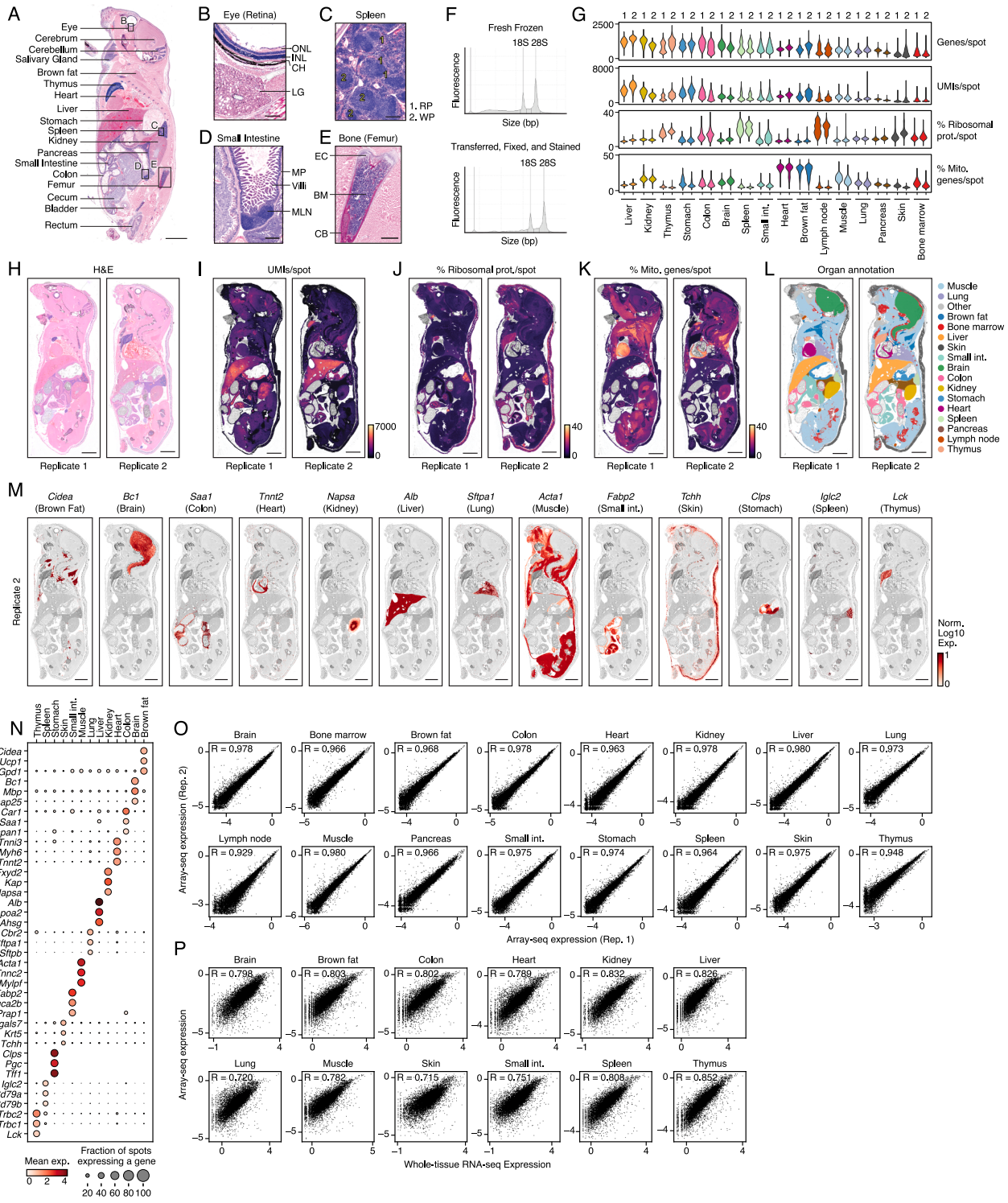

(legend on next page)

Figure S1. Whole-mouse histological sectioning and Array-seq data metrics and reproducibility, related to Figure 1

(A) H&E-stained, whole-mouse section (10 μm thickness) from a single 6-week-old animal with organs indicated.

(B–E) Magnified images of the insets from (A) depicting histologic structures of the eye (B), spleen (C), small intestine (D), and bone (E).

(F) Representative total RNA quality from a fresh frozen mouse tissue section (thymus is shown) with (bottom) or without (top) transfer with cryofilm, followed by methanol fixation and H&E staining.

(G) Distribution of genes/spot, UMIs/spot, and percentages of reads mapped to ribosomal protein or mitochondrial genes per spot for the indicated organs across the two whole-mouse section datasets.

(H–L) Two independent mice (rows) were sectioned, stained with H&E, and imaged (H). Grayscale H&E images were overlaid with unique molecular identifier (UMI) counts per spot (I), percentages of reads mapped to ribosomal protein (J) or mitochondrial (K) genes, and clustering data labeled with indicated organs (L).

(M) Scaled $\log_{10}$ expression values of indicated marker genes across organs (columns) overlaid on grayscale H&E images for a whole-mouse section from the Array-seq dataset.

(N) Expression of marker genes (rows) differentially expressed across organs (columns) is shown as percent of spots in which a gene is detected (circle) and mean expression across spots (color scale).

(O and P) Correlation (Pearson's coefficient) between independent whole-mouse Array-seq profiles (O) or average Array-seq and whole-tissue, bulk RNA-seq datasets (P) for the indicated organs. Shown are the normalized $\log_{10}$ unique molecular identifier (UMI) counts, which were averaged across all spots for each gene across each replicate (O) or both replicates (PD) and across independent organ samples (n = 4 independent mice) for bulk, whole-tissue RNA-seq data (P).

Scale bars: 5 mm (A and H–M); 250 μm (B–D); 500 μm (E).

Norm, normalized; Exp, expression; Int, intestine; Ribo, ribosomal; Mito, mitochondrial.

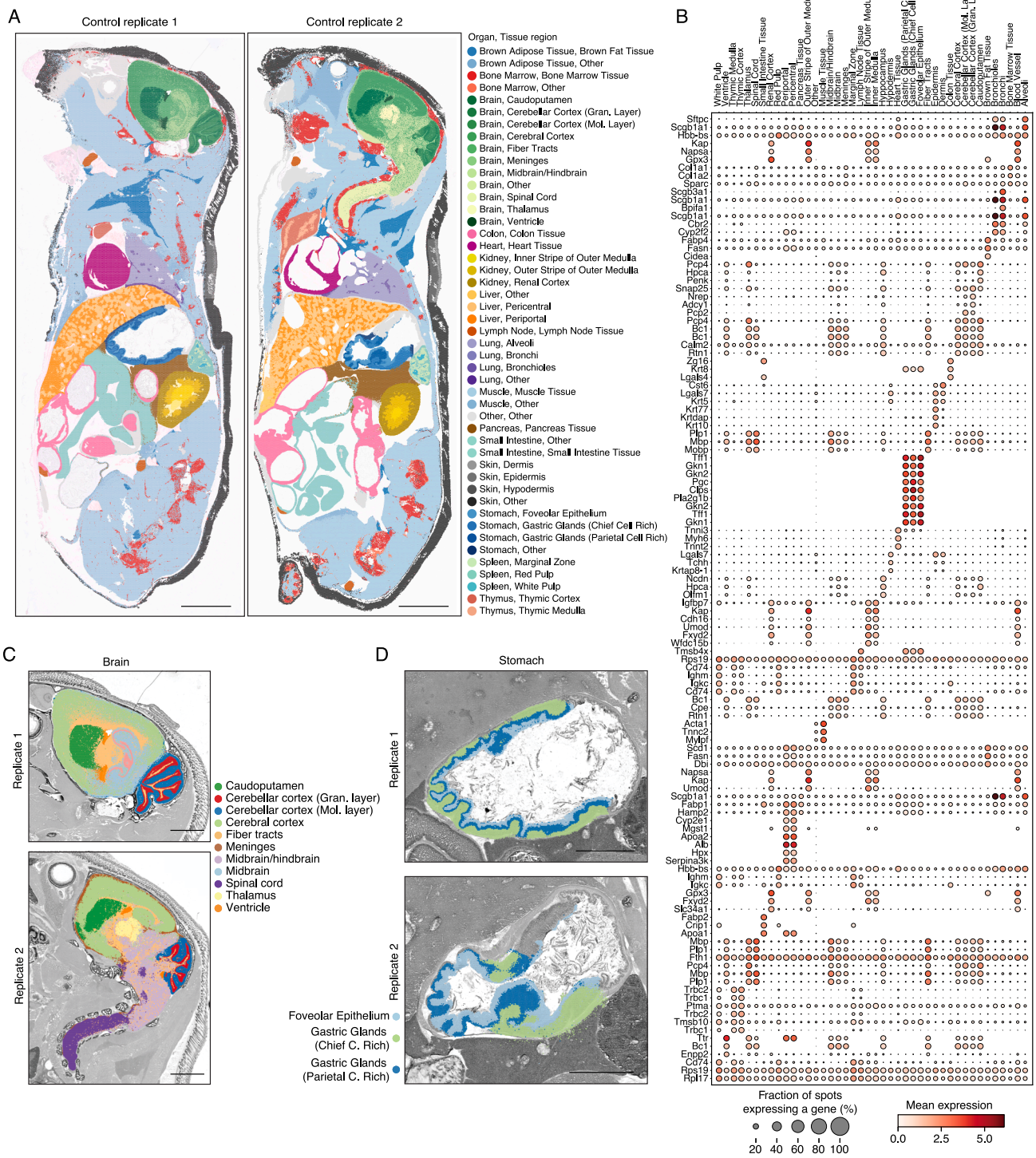

Figure S2. Whole-mouse Array-seq data accurately delineates tissue regions across the body, related to Figure 1

(A) Shown are grayscale images of two H&E-stained, whole-mouse sections (replicates) overlaid with indicated organs and tissue regions identified by clustering analysis of the spatial expression data.

(B) Expression of marker genes (rows) differentially expressed across tissues (columns) shown as percent of spots in which a gene is detected (circle) and mean expression across spots (color scale).

(legend continued on next page)

(C and D) Magnified images of the brain (C) and stomach (D) showing grayscale H&E staining overlaid with histological subregions of each organ type (colors) per replicate.
Scale bars: 5 mm (A); 1 mm (C and D).
Gran, granular; Mol, molecular; C, cell.

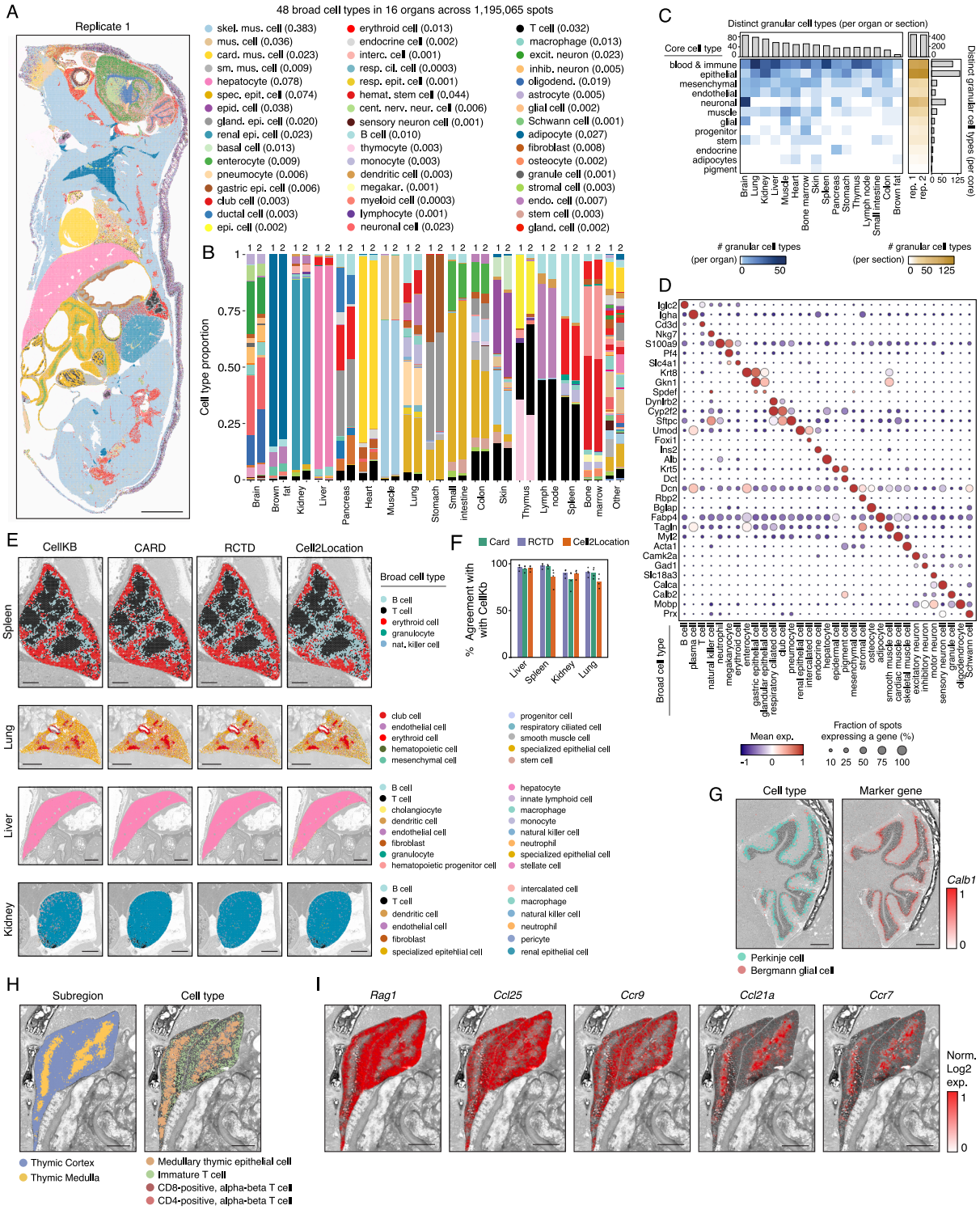

Figure S3. Organism-wide, spatial annotation of cell types using whole-mouse Array-seq, related to Figure 2

(A) Spatial annotation of mouse cell types across 16 organ systems in the whole-mouse section from replicate 1 of the Array-Seq dataset. For visualization, cell types with the highest inferred proportion per spot were assigned to each spot. Shown are broad cell types according to our in-house classification (Table S1C; STAR Methods). Numbers in parentheses indicate the proportion of each cell type across whole-mouse sections from both replicates. Replicate 2 is shown in Figure 2B.

(legend continued on next page)

(B) Stacked bar plot of the proportion (*y* axis) of indicated broad cell types based on our classification (Table S1C; STAR Methods) across indicated organs (*x* axis) per replicate (top).
(C) Count of distinct granular cell types per core cell type (rows; classifications in Table S1C and STAR Methods) across 16 organs (left heatmap) or whole-body sections (right heatmap). Both heatmaps display the twelve most abundant core cell type groups by proportion in the dataset. The top bar plots show the total number of distinct granular cell types across the indicated core cell types per organ (left) or the total number of distinct granular cell types spanning all core cell types across whole-body sections (right).
(D) Expression of marker genes (rows) differentially expressed across broad cell types (columns) shown as percent of spots in which a gene is detected (circle) and scaled mean expression across spots (color scale).
(E and F) Benchmarking of CellKb for spot-level cell-type inference. (E) Broad cell-type assignments are overlaid on magnified grayscale organ images (rows) for each algorithm compared (columns). (F) Percent agreement between each algorithm and the top CellKb assignment per spot, shown by replicate (dots), for each organ.
(G) Magnified images of the brain cerebellum (Replicate 2) showing grayscale images of H&E staining overlaid with indicated cell types (left) and scaled $\log_{10}$ expression of the *Calb1* gene (right).
(H and I) Thymus cell-type and chemokine distributions. Shown are thymic regions (H, left), defined by clustering, and cell types (H, right), and expression of indicated genes (I).
Scale bars: 5 mm (A); 500 μm (E, spleen); 2 mm (E, lung); 2.5 mm (E, liver); 1.5 mm (E, kidney); 1 mm (G–I).
Skel, skeletal; Mus, muscle; Card, cardiac; Sm, smooth; Spec, specialized; Epi, epithelial; Epid, epidermal; Gland, glandular; Interc, intercalated; Resp, respiratory; Hemat, hematopoietic; Cent, central; Nerv, nervous; Neur, neuronal; Megakar, megakaryocyte; Excit, excitatory; Inhib, inhibitory; Oligodend, oligodendrocyte; Endo, endothelial; Rep, replicate; Nat, natural; Norm, normalized; Exp, expression.

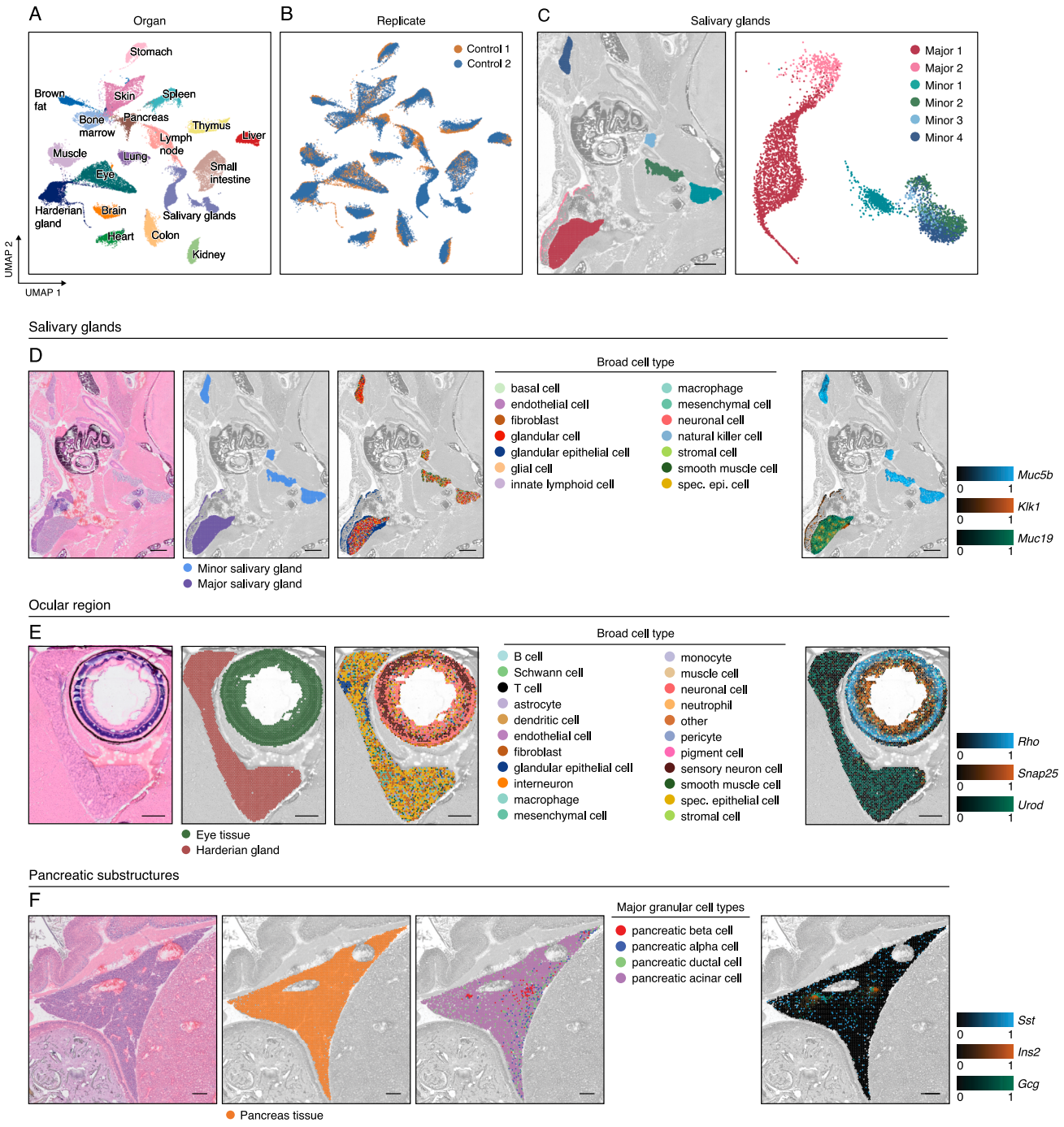

Figure S4. Identification of finer structures and specialized tissue domains across the body, related to Figure 2

(A and B) UMAP of reclustered, downsampled spots from the 16 annotated organs, together with spots originally labeled as "other." Points are colored by cluster, indicating original organ identities and additional structures present within the "other" group (A), or by replicate (B).

(C) Major and minor salivary glands overlaid on the grayscale H&E image from the spatial transcriptomics data (left) and shown in a zoomed inset of the UMAP from (A), displaying only salivary gland spots (right).

(D) H&E image showing salivary gland tissue (left); salivary gland tissue overlaid with salivary gland spots colored by major or minor gland type (center-left); broad cell-type annotations per spot (center-right); and scaled $\log_{10}$ expression of the indicated marker genes (right).

(E) H&E image showing the eye and harderian gland (left); eye and harderian gland tissue overlaid with spots colored by eye or harderian gland identity (center-left); broad cell-type annotations per spot (center-right); and scaled $\log_{10}$ expression of the indicated marker genes (right).

(legend continued on next page)

(F) H&E image of the pancreas (left); pancreatic tissue overlaid with tissue spots colored by pancreatic tissue identity (center-left); granular cell types involved in islet function and exocrine organization (center-right); and scaled normalized log_{10} expression of pancreatic islet marker genes (right).
Scale bars: 1 mm (C and D); 500 μm (E and F).
Spec, specialized; Epi, epithelial.

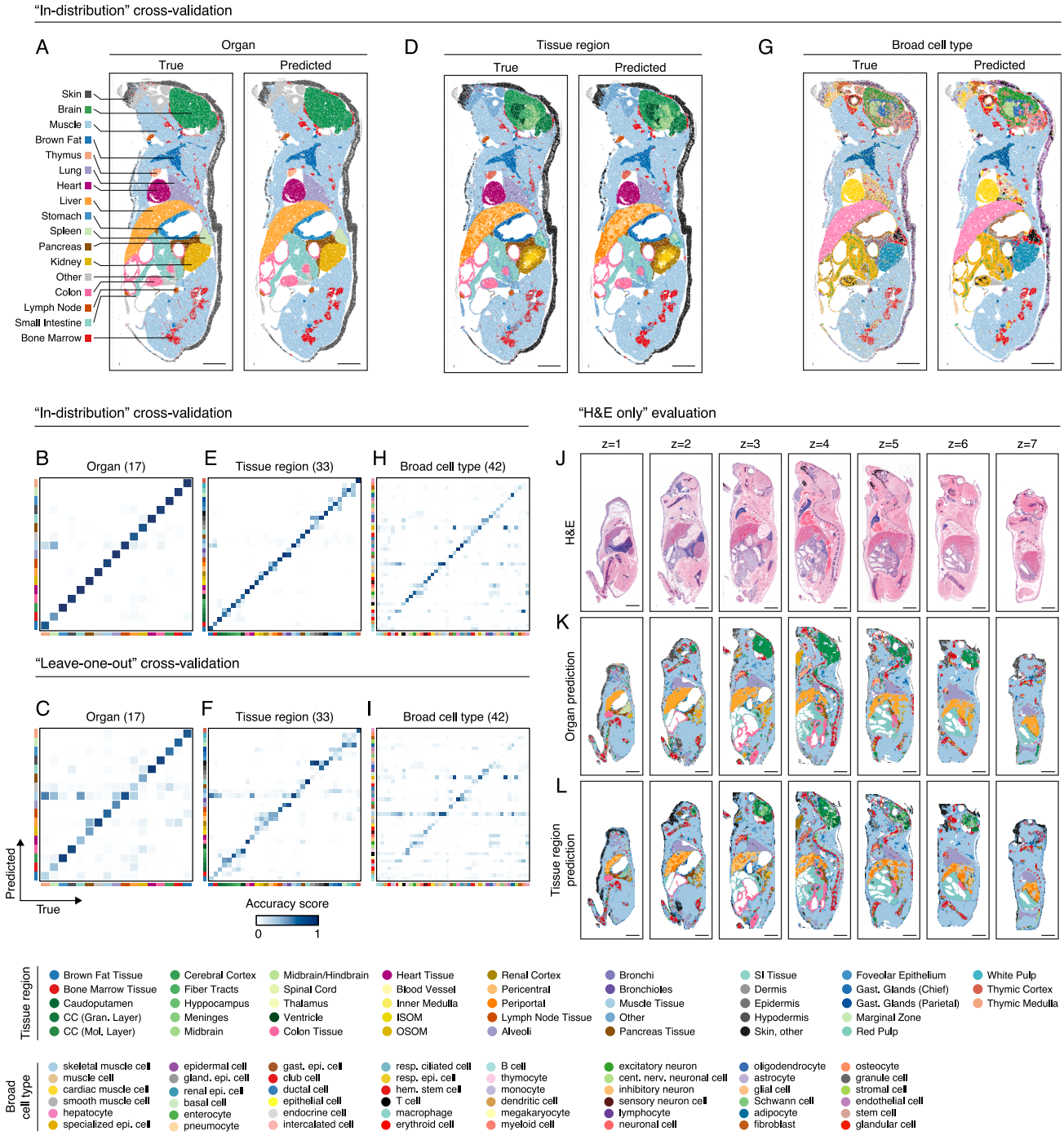

Figure S5. Performance of the LABEL model for virtual staining of H&E images, related to Figure 3

(A–C) Cross-validation of the LABEL model for organ prediction using Array-seq annotated H&E images.

(A) Whole-mouse spatial transcriptomics section evaluated using the "in-distribution" cross-validation approach (STAR Methods), shown with ground truth and LABEL-predicted organ identities.

(B) Normalized confusion matrix for the "in-distribution" approach in (A).

(C) Normalized confusion matrix for the "leave-one-out" approach (STAR Methods).

(D–F) Cross-validation of the LABEL model for tissue region prediction.

(D) Whole-mouse spatial transcriptomics section evaluated using the "in-distribution" cross-validation approach (STAR Methods), shown with ground truth and LABEL-predicted tissue region identities.

(E) Normalized confusion matrix for the "in-distribution" approach in (D).

(legend continued on next page)

(F) Normalized confusion matrix for the ''leave-one-out'' approach (STAR Methods).
(G–I) Cross-validation of the LABEL model for broad cell-type prediction.
(G) Whole-mouse spatial transcriptomics section evaluated using the ''in-distribution'' cross-validation approach (STAR Methods), shown with ground truth and LABEL-predicted broad cell-type identities.
(H) Normalized confusion matrix for the ''in-distribution'' approach in (G).
(I) Normalized confusion matrix for the ''leave-one-out'' approach (STAR Methods).
All ''in-distribution'' cross-validation was shown for the evaluation of spots from control replicate 1 that were excluded from training (A-B, D-E, G-H), and all ''leave-one-out'' cross-validation was shown for all spots from control replicate 1 when the entire section was held out of training (C, F, and I).
(J–L) H&E-stained, whole-mouse sections (10 μm thickness), as shown in Figure 3E, from a single 6-week-old animal and at various depths (J) used for independent testing of LABEL for the annotation of (K) organ or (L) tissue regions.
Scale bars: 5 mm (A, D, G, and J–L).
ISOM, inner stripe of outer medulla; OSOM, outer stripe of outer medulla; Gast, gastric; TH, thymus; SP, spleen; SK, skin; SI, small intestine; PN, pancreas; MU, muscle; LU, lung; LN, lymph node; LI, liver; KI, kidney; HE, heart; CO, colon; BR, brain; BM, bone marrow; BF, brown fat; Gran, granular; Mol, molecular; C, cell.

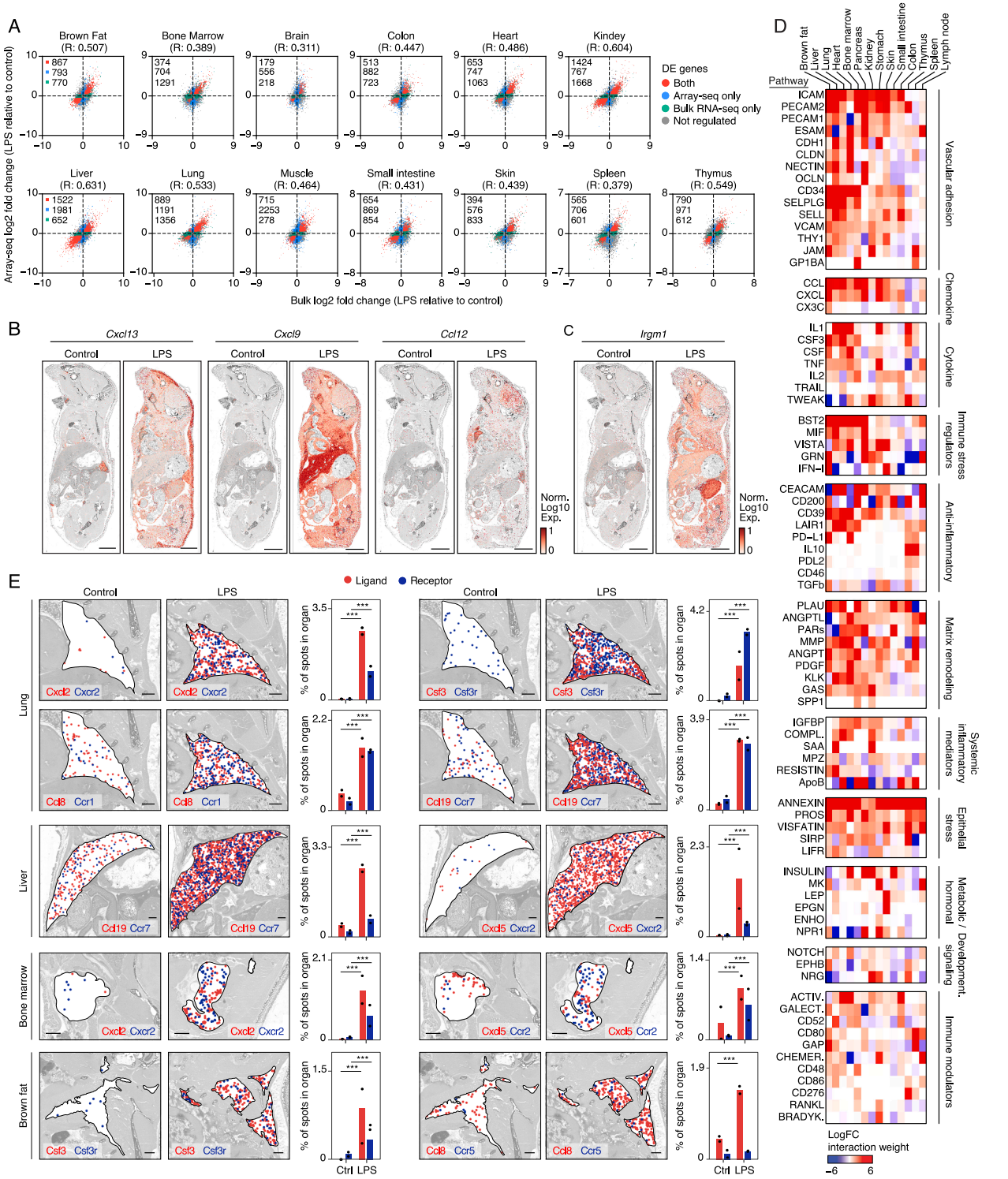

Figure S6. Gene regulation and ligand-receptor signaling across tissues during endotoxemia, related to Figure 4

(A) Dot plots showing $\log_2$ fold-change in gene expression in organs processed by bulk RNA-seq (*x* axis) or annotated in whole-mouse Array-seq data (*y* axis) from animals at 12 h post-sublethal LPS injection relative to matching untreated mice. Colored dots represent genes regulated in Array-seq data only (blue), whole-tissue, bulk data only (green), or both (orange).

(B and C) Grayscale images of H&E-stained, whole-mouse sections from mice at 12 h post-sublethal LPS injection (5 mg/kg) or left untreated as controls overlaid with scaled $\log_{10}$ expression of indicated genes. Scale bars: 5 mm.

(legend continued on next page)

(D) Heatmap of inferred signaling pathways (rows) across organs (columns) shown as $\log_2$ fold-change in interaction weight in LPS-treated mice relative to controls from the Array-seq dataset. Pathways shown are significantly altered in at least one organ.
(E) Spatial visualization of selected ligand-receptor pairs across representative organs, showing ligand (red) and receptor (blue) expressing spots overlaid on grayscale H&E images from control and LPS-treated mice. The percentage of spots expressing each ligand or receptor is quantified per organ and per replicate. Statistical significance was assessed using Fisher's exact test with Benjamini-Hochberg correction. ***$p < 0.001$. Scale bars: 1 mm.
Norm, normalized; Exp, expression; Ctrl, control; COMPL, complement; BRADYK, bradykinin; CHEMER, chemerin.

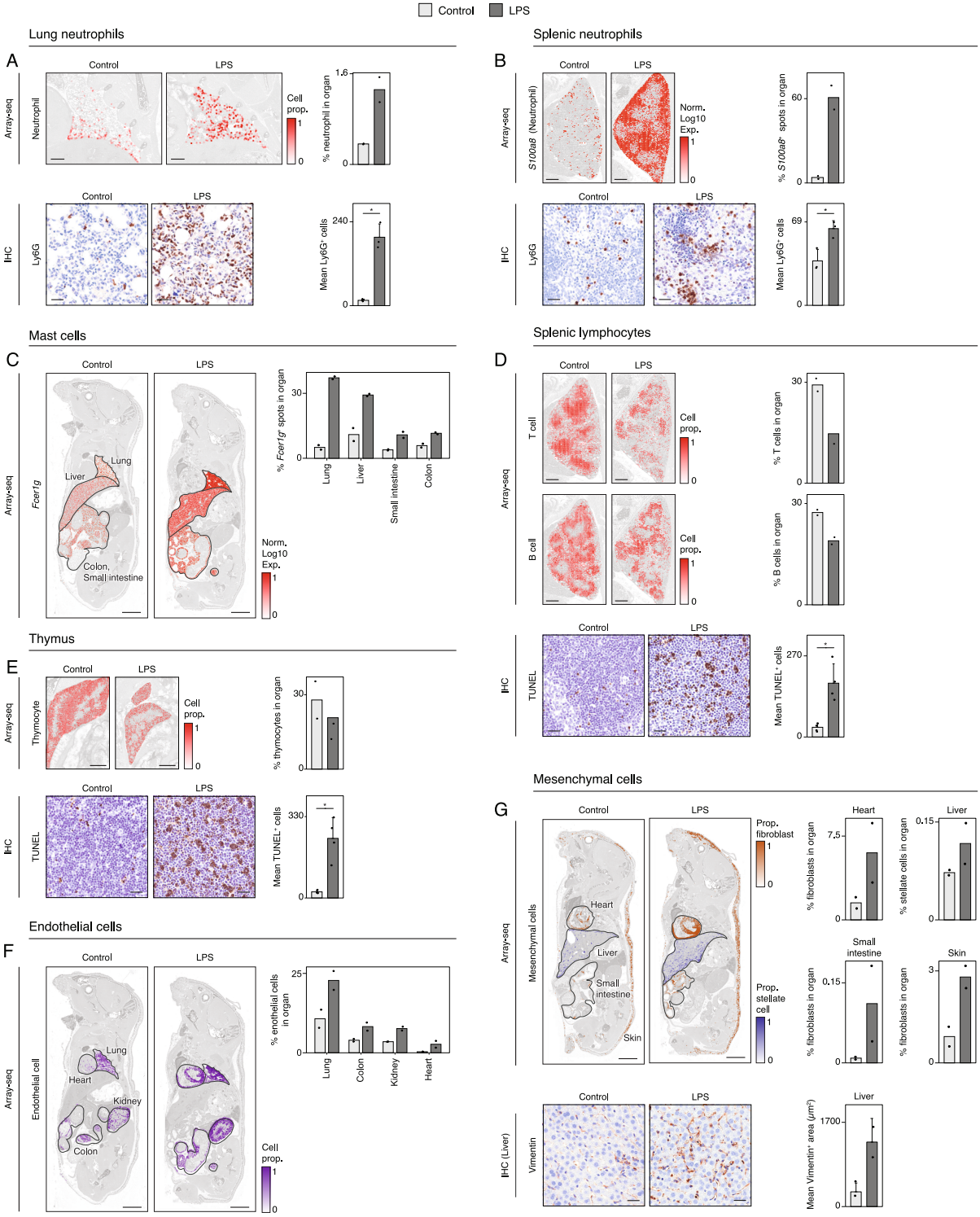

Figure S7. Changes in cell-type abundance across organs during systemic inflammation, related to Figure 5

(A) Grayscale H&E-stained lung tissue from the whole-mouse Array-seq dataset overlaid with the proportion of identified neutrophils per spot (top), and Ly6G immunohistochemistry validation in an independent cohort of LPS-treated and control mice (n = 3 independent mice per group) (bottom). Quantification of neutrophil abundance or mean Ly6G⁺ cells per field for each biological replicate is shown adjacent to each set of images (STAR Methods).

(legend continued on next page)

(B) Grayscale H&E-stained spleen tissue from the whole-mouse Array-seq dataset overlaid with $\log_{10}$ S100a8 expression per spot (top) and Ly6G immunohistochemistry validation in an independent cohort of LPS-treated and control mice ($n = 3$ independent mice per group) (bottom). Quantification of S100a8$^+$ spots or mean Ly6G$^+$ cells per field for each biological replicate is shown adjacent to each set of images.
(C) Grayscale H&E-stained whole-mouse sections from the Array-seq dataset showing $\log_{10}$ Fcer1g expression per spot in the lung, liver, colon, and small intestine, with quantification of the percentage of Fcer1g$^+$ spots in each organ.
(D) Grayscale H&E-stained spleen tissue from the whole-mouse Array-seq dataset showing the proportion of T cells per spot (top) and B cells per spot (middle), with quantification of abundance shown adjacent. Below is shown TUNEL staining of spleen tissue from an independent cohort of LPS-treated and control mice ($n = 4$ independent mice per group). Quantification of mean TUNEL$^+$ cells per field for each biological replicate is shown adjacent.
(E) Grayscale H&E-stained thymus tissue from the whole-mouse Array-seq dataset showing the proportion of thymocytes per spot, with quantification of thymocyte abundance shown adjacent. Below is shown TUNEL staining of thymus tissue from an independent cohort of LPS-treated and control mice ($n = 4$ independent mice per group). Quantification of mean TUNEL$^+$ cells per field for each biological replicate is shown adjacent.
(F) Grayscale H&E-stained whole-mouse sections from LPS-treated and control mice showing the proportion of endothelial cells per spot in the lung, heart, kidney, and colon, with quantification of abundance per organ.
(G) Grayscale H&E-stained whole-mouse sections from LPS-treated and control mice showing the proportion of fibroblasts and stellate cells per spot in the heart, liver, small intestine, and skin (top), with quantification of abundance shown adjacent. Below is shown vimentin staining of liver tissue from an independent cohort of LPS-treated and control mice ($n = 2$ independent mice per group). Quantification of mean vimentin$^+$ area per field for each biological replicate is shown adjacent.
Statistical comparisons between LPS-treated and control groups for all immunohistochemistry quantifications used a one-sided Mann-Whitney U test. $^*p < 0.05$. Error bars, SD (A, B, D, E, and G). Scale bars: 1 mm (A, top; E, top); 25 μm (A, bottom; B, bottom; D, bottom; E, bottom; and G, bottom); 500 μm (B, top; D, top, center); 5 mm (C, F, and G, top).
Norm, normalized; Exp, expression.

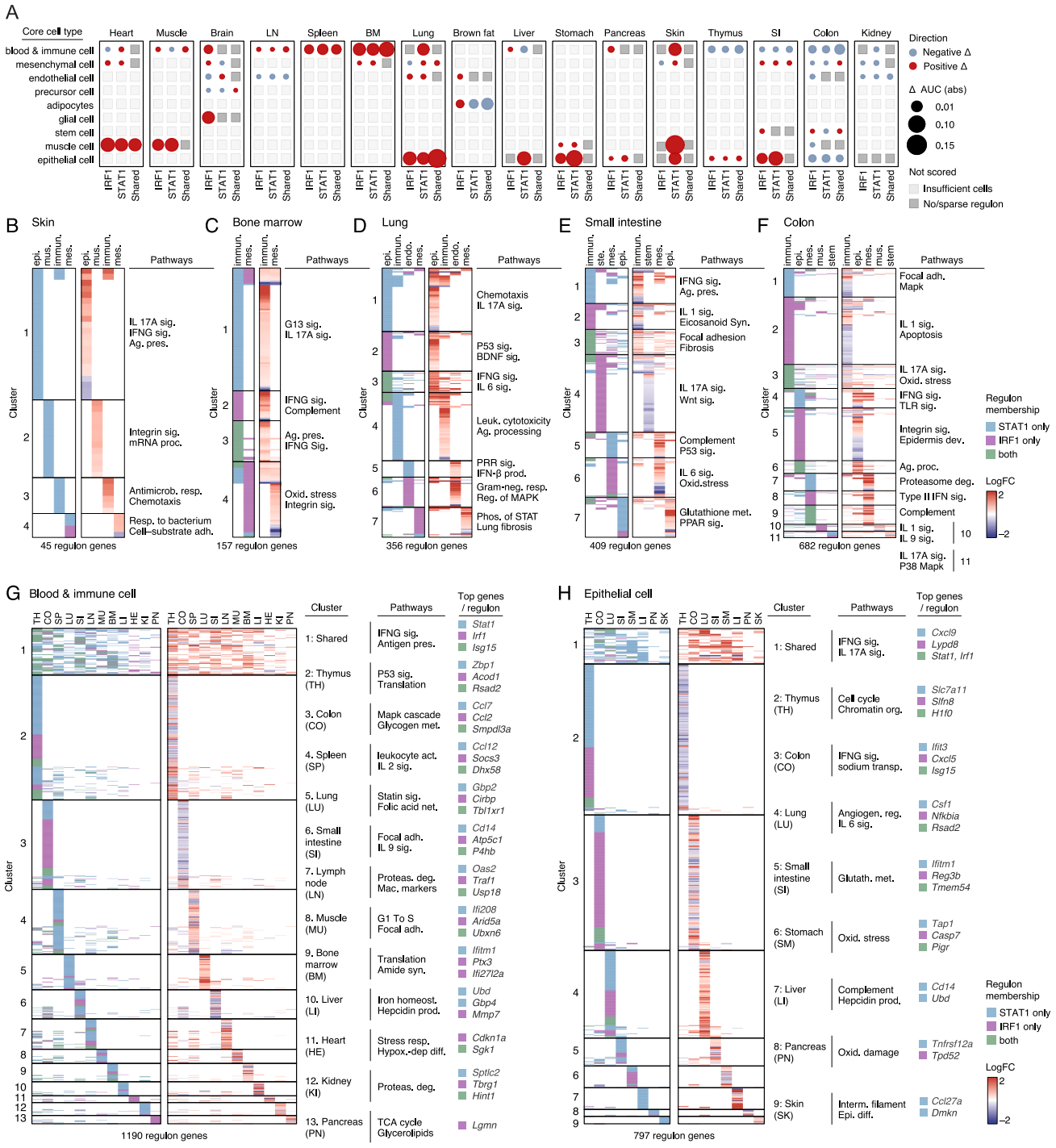

Figure S8. STAT1- and IRF1-driven transcriptional programs across organs and cell types in endotoxemia, related to Figure 7

(A) Heatmap showing activity scores as ΔAUCell values for STAT1, IRF1, and shared STAT1/IRF1 regulons across organs and core cell types, where ΔAUCell represents the difference between the mean AUCell score in LPS-treated and control mice. Only regulons significantly enriched for IRF1 or STAT1 motifs (NES $\geq$ 3.2, Q $\leq$ 0.001) are shown.

(B–F) Heatmaps of $\log_2$ fold change (LPS relative to control) for genes (rows) belonging to STAT1, IRF1, or shared regulons in the indicated organs. Rows are first grouped by regulon membership (STAT1-only, IRF1-only, shared) and, within each group, hierarchically clustered by $\log_2$ fold change. Columns represent core cell types from each organ. Enriched pathways corresponding to each regulon cluster are shown to the right.

(G and H) Heatmaps of $\log_2$ fold change (LPS relative to control) for genes belonging to STAT1, IRF1, or shared regulons in blood and immune cells (G) or epithelial cells (H), shown across organs (columns). Rows are grouped by regulon gene sets that are shared across multiple organs ("shared") or that are predominantly

(legend continued on next page)

organ-specific and hierarchically clustered within each group by regulon membership and $\log_2$ fold change. Enriched pathways and top differentially expressed genes from each regulon are indicated for each group.

Sig, signaling; Ag, antigen; pres, presentation; Proc, processing; antimicrob, antimicrobial; Resp, response; Adh, adhesion; Oxid, oxidative; Leuk, leukocyte; Prod, production; Reg, regulation; Phos, phosphorylation; Syn, synthesis; Dev, development; Deg, degradation; Met, metabolism; Mac, macrophage; Dep, dependent; Diff, differentiation; Org, organization; Glutath, glutathione; Interm, Intermediate; Epi, epidermis.